



**The International Congress for
global Science and Technology**



**ICGST International Journal on Graphics, Vision
and Image Processing (GVIP)**

**Volume (16), Issue (III)
December 2016**

**www.icgst.com
www.icgst-amc.com
www.icgst-ees.com**

**© ICGST, 2016
Delaware, USA**

GVIP Journal
ISSN Print 1687-398X
ISSN Online 1687-3998
ISSN CD-ROM 1687-4005
© ICGST 2016

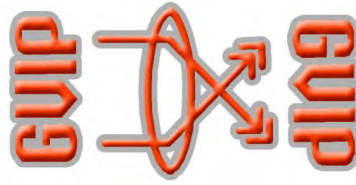


Table of Contents

Papers	Pages
P1151637518, Author="Géraud Aزهoun-Pazou and Kokou Assogba", Title="Automatic Recognition of Lesion-like Regions in Black Skin Medical Images"	1--7
P1151636515, Author="Khalid A. Al-Afandy and EL-Sayed M. EL-Rabaie and Fathi E. Abd El-Samie and Osama S. Faragallah and Ahmed ELmhalaway and A. M. Shehata", Title="Robust Color Image Watermarking Technique Using DWT and Homomorphic based SVD"	9--18
P1151638519, Author="TALLURI. SUNIL KUMAR and T.V.RAJINIKANTH and B. ESWARA REDDY", Title="Region Based Integrated Approach for Image Retrieval"	19--29
P1151616490, Author="Rafika Ben Salem and Karim Saheb Ettabaa and Mohamed Ali Hamdi", Title="Spectral-Spatial Classification of Hyperspectral Image based on Oversampling and Multi-Feature Kernels"	31--40



**ICGST International Journal on Graphics, Vision and Image Processing
(GVIP)**

**A publication of the International Congress for global Science and Technology -
(ICGST)**

ICGST Editor in Chief: Dr. rer. nat. Ashraf Aboshosha

www.icgst.com, www.icgst-amc.com, www.icgst-ees.com

editor@icgst.com



Automatic Recognition of Lesion-like Regions in Black Skin Medical Images

G. Azehou-Pazou, K. Assogba

LETIA, Polytechnic School of Abomey-Calavi, 01 BP 2009, Abomey-Calavi, Rep. Benin

geraud.pazou@gmail.com, mkokouassogba@yahoo.fr

Abstract

This paper presents a study made to automatically recognize lesion-like regions in black skin medical images. Skin lesions have consistently had one of the most rapidly increasing incidences of all cancers. Early diagnosis is particularly important but it is a challenging task, especially for black populations. Moreover, black skin specialists are often limited to the use of classic macroscopic images for diagnosis purpose. All these difficulties are related to black skin pigmentation level and the small visual differences between lesion parts and healthy ones.

We propose here a computerized method which identifies automatically lesion regions with more accuracy and efficiency. It works like an automaton that traverse lesion images and automatically classifies healthy regions from lesions regions. The designed classifier is a Multi-Layer Perceptron Artificial Neural Network (MLP-ANN) trained with color and texture features. We made many combinations of features and varied the number of neurons in hidden layer, in order to obtain best performances. Nine features (six of texture and three of color) have been retained to train the network. The achieved classification performance is 97.2% in both training, validation and testing set. ¹

Keywords: Medical images, Black skin, Neural Network, Lesion recognition, Texture features.

Nomenclature

ANN	Artificial Neural Network
CAD	Computer Aided Diagnosis
MLP	Multi-Layer Perceptron
MLP-ANN	Multi-Layer Perceptron type Artificial Neural Network
CADS	Computer Aided Diagnosis System
PPV	Positive Predictive Value or Precision
NPV	Negative Predictive Value
TPR	True Positive rate or Sensitivity
SPC	Specificity or True Negative Rate

¹ This study has been implemented on Matlab Neural Network Toolbox software at LETIA lab. University of Abomey-Calavi in Republic of Benin

FPR	False Positive Rate
ACC	Accuracy
FP	False Positive
FN	False negative
TP	True Positive
TN	True Negative

1. Introduction

Dermatology is one of the fields where medical images have been used for years, since their potential benefits had been revealed in 1992 by Stoecker and Moss [1]. However, many parameters such as: type and quality of images, noise, or acquisition techniques influence image processing. About that, black skin images are certainly one for which difficulties occur most. In fact, while several studies proved the effectiveness of dermoscopic images based diagnosis [2-5], dermoscopy is ineffective in black skin and then unusable by black skin specialists. Therefore, these specialists are limited to the use of standard digital cameras as acquisition devices. Once images are acquired, major difficulties appear regarding their processing.

Indeed, in black skin, there is the presence of pigment throughout the basal layer of epidermis [6]. Therefore, the approach with black population is quite different, even if diagnostic procedure is generally the same, regardless of skin color [7]. So, it is important to make research in the direction of setting up Computer Aided Diagnosis (CAD) systems specific to black skin. In this context, we proposed in a previous paper, a method to analyze black skin macroscopic medical images. In that work, we focused on preprocessing and segmentation using a combination of mathematical morphology and edge detection [8]. The method improved edge detection but had also shown its limits. So, further studies deserved to be undertaken in order to develop a more efficient system.

With the significant advances occurred during recent years in the field of computer science and artificial intelligence, medical images processing has become more reliable and accurate [9]. Some good applications can be found in [10], [11] [12] and [13]. Artificial Neural Networks (ANNs) in particular, have been used to solve many image processing problems, as reported in [14], [15]



and [16]. Among them, we can enumerate: applications of ANNs in pre-processing step [17-19]; ANNs trained to perform segmentation task [20-22]. ANNs have also been used in medical diagnosis as main stage of a CADs [23]. Despite these advances, there exist very few studies on the subject of black skin, as regards the development of CADs. The typical pipeline adopted for automated skin lesion diagnosis is: image acquisition, artifact detection, lesion segmentation, feature extraction and classification [24]. In this paper, we propose a neural network based classifier acting in the artifact detection stage. It has been trained with color and texture features and works like an automaton that traverse black skin lesion images and automatically differentiates healthy regions from lesions regions.

The remainder of the paper is organized as follows: Section (2) discusses the theory about feedforward type neural networks; Section (3) emphasizes on the material and the methods used in this work; In Section (4) we present the results and make some discussions and finally, we conclude in Section (5).

2. Theory

An Artificial Neural Network is a computational system inspired by the structure, the processing method and the learning ability of a biological brain. It is characterized by a large number of very simple neuron-like processing elements, a large number of weighted connections (links) between these elements and a distributed representation of knowledge over the connections [25]. Knowledge is acquired by the network through a learning process [26]. ANNs' expansion started in 1943 when McCulloch and Pitts proved that neuron can have two states and that those states could be dependent on some threshold value [27]. Since then, ANNs have been widely used in research because they can model highly non-linear systems in which the relationship among the variables is unknown or very complex [28]. A review of various classes of neural networks can be found in [29] and [30]. Multilayer perceptrons (MLPs) are the most popular type of neural networks in use today. They belong to a general class of structures called feedforward neural networks, a basic type of neural network capable of approximating generic classes of functions, including continuous and integrable functions [31].

MLP Structure: In MLP structure, neurons are grouped into layers. The first and last layers are called input and output layers respectively, because they represent inputs and outputs of the overall network. The remaining layers are called hidden layers. Typically, an MLP neural network consists of an input layer, one or more hidden layers, and an output layer, as shown in Figure 1.

Mathematical background: Suppose the total number of layers is L . The 1st layer is the input layer, the ℓ^{th} layer is the output layer, and layers 2 to $L-1$ are hidden layers. Let the number of neurons in ℓ^{th} layer be N_ℓ , $\ell = 1, 2, \dots, L$ and w_{ij}^ℓ represent the weight of the link between j^{th} neuron of $\ell-1^{\text{th}}$ layer and i^{th} neuron of ℓ^{th} layer, $1 \leq j \leq N_{\ell-1}$, and $1 \leq i \leq N_\ell$. Let x_i represent the i^{th} external input to the MLP, and z_i^ℓ be the output of i^{th}

neuron of ℓ^{th} layer. An extra weight parameter w_{i0}^ℓ is introduced for each neuron, representing the bias for i^{th} neuron of ℓ^{th} layer. As such, \mathbf{w} of MLP includes w_{ij}^ℓ , $j=0, 1, \dots, N_{\ell-1}$, $i=1, 2, \dots, N_\ell$, $\ell=2, 3, \dots, L$. \mathbf{w} expression is given by equation (1):

$$\mathbf{w} = [w_{10}^2 \ w_{11}^2 \ w_{12}^2 \ \dots \ w_{N_L N_{L-1}}^L]^T \quad (1)$$

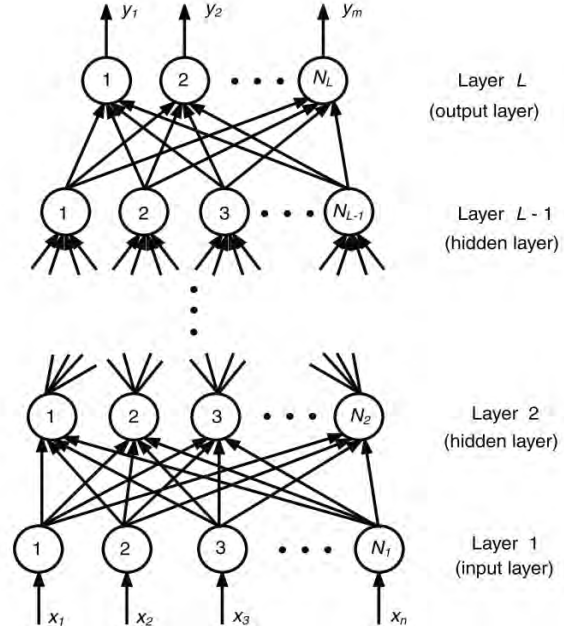


Figure 1. Multilayer perceptron (MLP) Neural Network structure

In a neural network, each neuron with the exception of neurons at the input layer receives and processes stimuli (inputs) from other neurons. The processed information is available at the output end of the neuron. A neuron of the ℓ^{th} layer receives stimuli from neurons of $\ell-1^{\text{th}}$ layer, that is: $h_{\ell-1}^{\ell-1}, h_{\ell-2}^{\ell-1}, \dots, h_{N_{\ell-1}}^{\ell-1}$. Each input is multiplied by the corresponding weight parameter, and resulting products are added to produce a weighted sum γ_i^ℓ (cf. equation 3).

This weighted sum is passed through a neuron activation function σ to produce the final output h_i^ℓ of the neuron (cf. equation 2). This output represents the hypothesis (or assumption) of the neuron, and it can become the stimulus for neurons in the next layer:

$$h_i^\ell = \sigma(\gamma_i^\ell) \quad (2); \quad \gamma_i^\ell = \sum_{j=0}^{N_{\ell-1}} w_{ij}^\ell h_j^{\ell-1} \quad (3)$$

Learning process: The purpose of ANN is to learn to recognize patterns in data. Once the neural network has been trained on samples data, it can make predictions by detecting similar patterns in future data. The process by which MLP neural network achieves learning or training is a two steps: feedforward and backpropagation.

In the feedforward process, the external inputs are first fed to the input neurons 1st layer, the outputs from the input neurons are fed to the hidden neurons of the 2nd layer, and so on, and finally the outputs of $L-1^{\text{th}}$ layer are



fed to the output neurons L^{th} layer. The difference between the resulting outputs and the expected ones is calculated to get the error. In backpropagation, errors that result from previous step are propagated back through the system, causing the system to adjust the connection weights. The training begins with random weights and the goal is to adjust them until the error is minimal. This is achieved by minimizing the objective function E of equation (4):

$$E = \frac{1}{2} \sum_{i=1}^m (h_i^L - y_i)^2 \quad (4)$$

More details about ANN learning process is available in [26].

3. Material and methods

Material: We implemented our programs and algorithms with MATLAB, Version 8.4 (R2014b). We designed, implemented and trained the network with the MATLAB neural network toolbox. Our data set includes 40 medical images which were taken in same conditions (cf. Table I).

Table I. Images Database Composition

Types of Images	Number
Erythema lesion	17
Tuberous Sclerosis Complex (TSC) lesion	6
Purpura lesion	5
Seborrheic Keratosis lesion	7
Eczema lesion	5
Images showing black people skin	20

These images were taken with a HD digital camera in the Dermatology service of the Hubert K. Maga University Hospital of Cotonou. Figure 2 shows samples from each type of skin lesion.

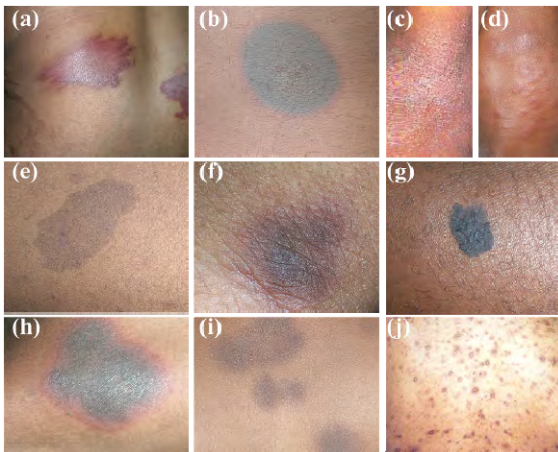


Figure 2. Some black skin lesions of our image database (a: Purpura lesion; c - j : Eczema lesion; e: TSC lesion; g: Seborrheic Keratosis; b - d - f - h - i : different types of Erythema)

We also downloaded images showing black people skin, from different online databases. From all these images, we extracted blocks of pixels of size 3x3, thanks to a program. Each block represents an example of the dataset (see figure 3 for extraction procedure). At the end, we obtained about 800.000 learning examples that we

divided into learning, validation and test sets, in the respective proportions of 60%, 20% and 20%.

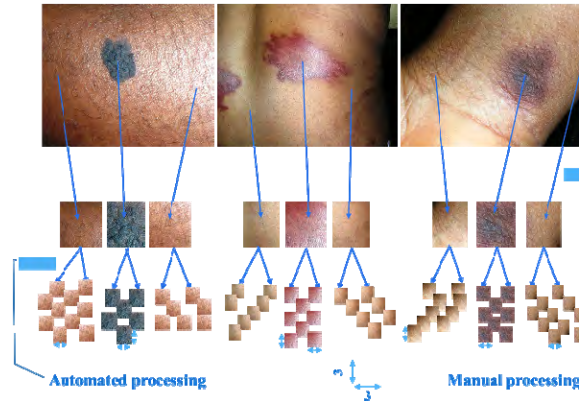


Figure 3. Regions extraction to blocks of pixels constitution

Methods: Normal skin regions are homogenous connected groups of pixels. So, color and texture information can be used to describe them. Fifteen features were identified to train the NN, but nine were finally retained. So the designed network has nine neurons in input layer and one in output layer. We varied the number of neurons in the hidden layer until we get the best performances. The input layer neurons correspond to features calculated for each example (3x3 pixel block). There are three color descriptors (one for each RGB color channel) and six texture descriptors.

Color features: We calculate the mean intensity value for each of the R, G and B channels (M_R , M_G and M_B) with formula (5).

- for each block $X(3,3)$,

$$M_k = \frac{1}{9} \sum_{i=1}^9 x(i) \quad (5), \quad k = \{R, G, B\}$$

Texture features: The retained texture features are: uniformity, standard deviation, skewness, kurtosis, smoothness, and entropy. They were chosen for their simplicity and efficiency. Let z_i represent the value of a pixel $x(i)$; features are defined as follows:

- Uniformity: it is maximum when all gray levels are equal (maximally uniform).

$$U = \sum_{i=1}^l p^2(z_i) \quad (6)$$

- Standard deviation: measure of average contrast.

$$\sigma = \sum_{i=1}^l (z_i - m)^2 p(z_i) \quad (7)$$

- Skewness: it is the measure of the asymmetry of the intensity values around the mean intensity.

$$s = \sum_{i=1}^l (z_i - m)^3 p(z_i) \quad (8)$$

- Smoothness: its value is 0 for regions of constant intensity and approaches 1 for regions with large excursions in the values of its intensity levels.



$$r = 1 - \frac{1}{1 + \sigma^2} \quad (9)$$

- Kurtosis: it is the measure of how outlier-prone a distribution is.

$$s = \sum_{i=1}^l (z_i - m)^4 p(z_i) \quad (10)$$

- Entropy: a measure of randomness.

$$e = - \sum_{i=1}^l p(z_i) \log_2 p(z_i) \quad (11)$$

With:

- l the number of possible intensity levels;
- z_i a random value of pixel intensity;
- $p(z_i)$ the histogram of intensity levels in a region around z_i ;
- and m the average intensity defined by:

$$m = \sum_{i=1}^l z_i p(z_i) \quad (12)$$

Network parameters: Activation function is the sigmoid function given by the formula (13).

$$\sigma(\gamma) = \frac{1}{1 + e^{-\gamma}} \quad (13)$$

Sigmoid function is a smooth switch function as shown by the curve of Figure 4. It has the property described by expression (14).

$$\sigma(\gamma) \rightarrow \begin{cases} 1 & \text{as } \gamma \rightarrow +\infty \\ 0 & \text{as } \gamma \rightarrow -\infty \end{cases} \quad (14)$$

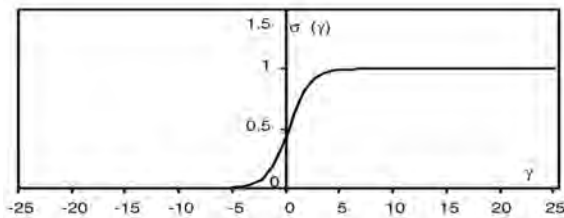


Figure 4. Sigmoid function.

Functioning of the proposed Technique: the designed classifier works like an automaton that traverses black skin lesion images and is able to differentiate healthy regions from lesions regions. So, when an image is input, the first step consists in dividing it into blocks of pixels of size 3x3. Then, features are calculated for each block and the equivalent function of the classifier is used to calculate the output. When the decision of the classifier is close to 1, all pixels values are replaced by 1. If, it's the contrary, values are replaced by 0. Thus, at the end we obtain a binary rebuilt image (cf. flowchart of figure 5).

The corresponding pseudocode of all this process is:

VARIABLES *InputImage*, *F*, *Features*[9], *NbOfBlocks*, *Blocks*[], *OutputImage*.

PREDEFINED FUNCTIONS *CalcFeatures*, *ComputeNN*, *ExtractBlocks*,

BEGIN

READ *InputImage*

DO [*NbOfBlocks*, *Blocks*] = *ExtractBlocks*(*InputImage*)

```
count = 0
WHILE count < NbOfBlocks
    count = count + 1
    Features = CalcFeatures(Blocks(count))
    F = ComputeNN(Features)
    If (0.5 < F <= 1) THEN
        Blocks(count) = 1
    ELSE
        Blocks(count) = 0
    ENDIF
ENDWHILE
WRITE OutputImage
END
```

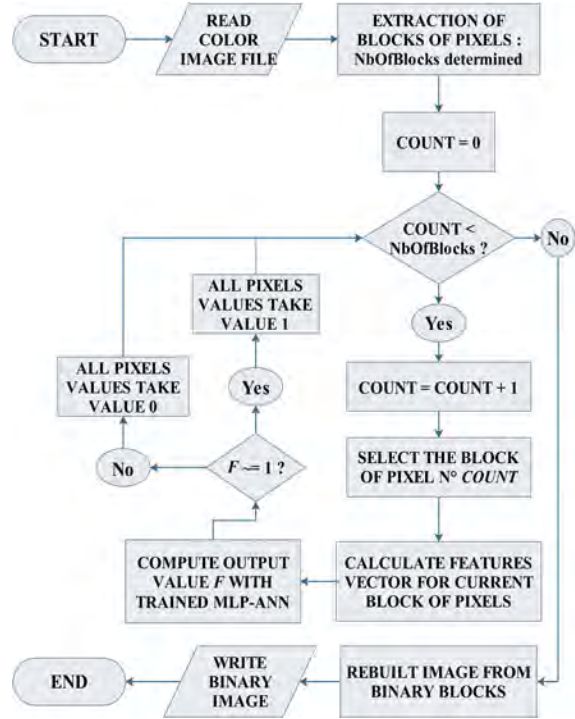


Figure 5. Flowchart of the proposed recognition technique

Evaluation metrics: We used six metrics to evaluate the performance of our classifier: Sensitivity, Specificity, Accuracy, False Positive Rate, Precision or Positive Predictive Value (PPV), Negative Predictive Value (NPV) and F1-Score. To define these metrics, let: TP (true positive) stand for the number of regions correctly classified as lesion region, TN (true negative) be the number of regions correctly classified as healthy regions, FP (false positive) the number of regions wrongfully classified as lesion and FN (false negative) be the number of regions classified as healthy but which are in reality lesion regions.

- Sensitivity or True Positive rate (TPR):

$$TPR = \frac{TP}{TP + FN} \times 100 \quad (15)$$

- False Positive Rate (FPR):

$$FPR = \frac{FP}{FP + TN} \times 100 \quad (16)$$

- Specificity (SPC) or True Negative Rate:



$$TPR = \frac{TN}{FP + TN} \times 100 \quad (17)$$

- Accuracy (ACC):

$$ACC = \frac{TP + TN}{TP + FN + FP + TN} \times 100 \quad (18)$$

- Precision or Positive Predictive Value (PPV):

$$PPV = \frac{TP}{FP + TP} \times 100 \quad (19)$$

- Negative Predictive Value (NPV):

$$NPV = \frac{TN}{FN + TN} \times 100 \quad (20)$$

4. Results and discussion

Results: We got best performances with six neurons in hidden layer. With this configuration, the network achieved his best validation performance after 457 iterations and the cross-entropy value of the objective function is around 0.083 (see Figure 6).

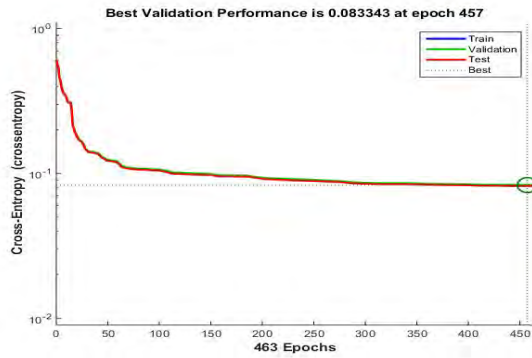


Figure 6. Training performance.



Figure 7. Confusion matrix.

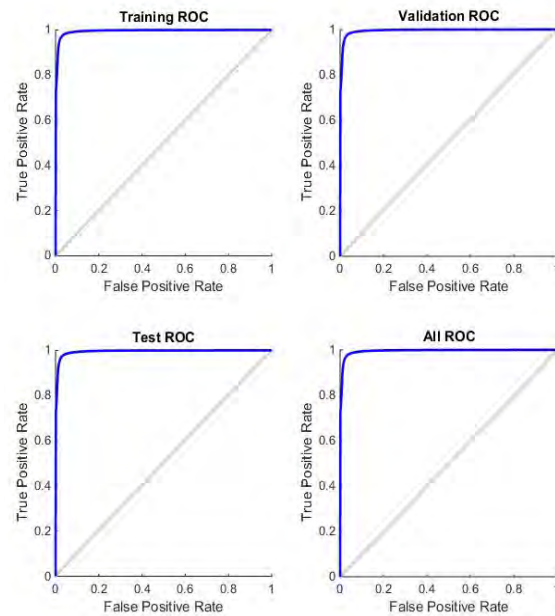


Figure 8. ROC Curves of the classifier.

The classification performance is good, considering error rates shown by confusion matrix of figure 7. Indeed, confusion matrix help to know percentages of samples which are misclassified in each set. According to the confusion matrix, the False Match Rate (FMR) in both training, validation and test stages is 2.8%. Moreover, the performance of the obtained classifier is more illustrated by the ROC curves of Figure 8. The form of ROC curve shows us that we have an excellent classifier if we refer to [32]. Indeed, the greater the area under the curve (AUROC) is, the better the classifier is [33]. Finally, the values of evaluation metrics are reported in Table II.

Table II. Values of Evaluation Metrics

Metrics	Values
True Positive Rate (TPR) or Sensitivity	96,9%
True Negative Rate or Specificity (SPC)	97,5%
False Positive Rate (FPR)	2,5%
Precision or Predictive Positive Value (PPV)	97,7%
Negative Predictive Value (NPV)	96,6%
Accuracy (ACC)	97,2%

Discussion: In our modelling, 1s stand for normal or healthy skin region and 0s for lesion regions. Thus, we can notice that 3.1% of normal skin regions are misclassified; whereas only 2.5% of lesion regions are misclassified. These values are satisfactory since low error rate in classification of lesion regions is particularly important for future segmentation purpose.

The sensitivity of the classifier is: 96,9 %; its Specificity is: 97,5% and the False Positive Rate (FPR) is: 2,5%. These values are significant, though poor to validate machine learning experiments [32]. So, to strengthen our results, the following values are considered: Precision or PPV: 97,7%; NPV: 96,6%; and Accuracy: 97,2%. Their high values (more than 95%) indicate a certain reliability.



However, our results need to be compared with results obtained by similar work, although there is no specific previous work with black skin in the literature, apart from ours published in [8]. For this purpose, two works have caught our attention: those of (Madan et al., 2011) and (Jafari et al., 2016). The first worked on the detection of acne-like regions in macroscopic medical images of face [13]. The second recently used deep learning to extract skin lesions from non-dermoscopic (macroscopic) images [22]. A comparison with our results is made in Table III on obtained values for three metrics used by both authors: best results are bold.

Table III. Comparison of Detection performances in Macroscopic Skin Images

Metrics	Papers or Works		
	Madan et al., 2011	Jafari et al., 2016	Our Work
Sensitivity	90,4 %	95,2 %	96,9 %
Specificity	88 %	98,8 %	97,5 %
Accuracy	89,2 %	98,5 %	97,2 %

Best results of specificity and accuracy are obtained by Jafari et al., whereas best sensitivity value is obtained by us. This shows that our recognition performances need to be improved, even if the gap is not very big. However, it is important to note that both works compared to ours, were performed on white skin. This could justify the best performances. Indeed, contrasts between healthy regions and lesions are much sharper in this kind of skin.

5. Conclusion

The major contribution of this article arise from the use of ANN for black skin lesions. Indeed, using MLP-ANN for recognition tasks is not new but finding the good learning features to achieve good performances is the main contribution of this research work. The trained classifier identifies lesion-like regions in black skin medical images. To do this, we first set up a dataset of size around 800.000 examples. Texture and color features have been calculated for each of these examples. After that, we trained the network, while varying the number of neurons in hidden layer in order to get best performances. Finally we obtained a very good classifier which is able to differentiate lesion regions from safe skin regions in medical images with a small error rate.

This study also allowed us to highlight the differences between black skin and white skin. These differences exist firstly in terms of color, secondly in anatomical and structural terms. They induce difficulties to dermatology practitioners, as seen in publications made on the subject. Texture and color information used here as learning parameters, confirms practices of black skin specialists, who usually resort to skin palpation (searching texture changes) and observation of color changes to make their diagnostics.

But, although the performances of the obtained classifier are good, error rate is not less considerable. This is why the developed technique is used in "artifact detection" stage. Thus, further processing have to be made on resulting images before segmentation.

6. Acknowledgements

We would like to thank Doctor Hugues ADEGBIDI of Hubert Maga National University Hospital (CNHU HKM) of Cotonou (Benin) for his valuable help in this work.

7. References

- [1] W. V. Stoecker, and R. H. Moss. Computerized Medical Imaging and Graphics. In Editorial: digital imaging in dermatology, 16(3), pp. 145–150. 1992.
- [2] A. Amelio, and C. Pizzuti. Skin lesion image segmentation using a color genetic algorithm. In Proceedings of the 15th annual conference companion on Genetic and evolutionary computation, pp. 1471-1478. 2013.
- [3] A. A. A. Al-abayechia, X. Guoa, W. H. Tana, and H. A. Jalabc. Automatic skin lesion segmentation with optimal colour channel from dermoscopic images. SCIENCEASIA, pp. 40, 1-7. 2014.
- [4] A. Pennisi, D. Bloisi, D. Nardi, A. R. Giampetruzzi, C. Mondino, & A. Facchiano. Melanoma detection using Delaunay triangulation. In IEEE 2015 27th International Conference on Tools with Artificial Intelligence (ICTAI), pp. 791-798. 2015.
- [5] M. E. Celebi, Q. Wen, S. Hwang, H. Iyatomi, and G. Schaefer. Lesion border detection in dermoscopy images using ensembles of thresholding methods. Skin Research and Technology, 19(1), pp. 252-258. 2013.
- [6] G. S. Puigdemont, R. N. Sintes, and T. Dieng. Dermatology with black skin patients. Euromedice. 2008.
- [7] D. Wallach. Specific aspects of dermatological diagnosis on black skin. In Rev. Pratt Review, pp. 3675-3688. 1981.
- [8] G. Azehou-Pazou, M. K. Assogba, and A. Vianou. A method of automatic black skin lesion's macroscopic image analysis. International Journal of Computer Applications & Information Technology, 4(1), pp. 9-14. 2013.
- [9] P. Wighton, T. K. Lee, H. Lui, D. I. Mclean, S. M. Atkins. Generalizing Common Tasks in Automated Skin Lesion Diagnosis. IEEE Transactions on Information Technology in Biomedicine, 15(4). 2011.
- [10] I. S. Akila, and V. Sumathi. Detection of Melanoma Skin Cancer using Segmentation and Classification Algorithm. In National Conference on Information and Communication Technologies (NCICT). 2015.
- [11] P. Rubegni, G. Cevenini, M. Burrioni, R. Perotti, G. Dell'Eva, P. Sbrano, ... & L. Andreassi. Automated diagnosis of pigmented skin lesions. International Journal of Cancer, 101(6), pp. 576-580. 2002.
- [12] V. H. Patil, D. S. Bormane, and V. S. Pawar. An automated computer aided breast cancer detection system. International Journal on Graphics, Vision and Image Processing, 6(1), pp. 69-72. (2006).
- [13] S. K. Madan, K. J. Dana, & O. Cula. Learning-based detection of acne-like regions using time-lapse features. In 2011 IEEE Signal Processing in Medicine and Biology Symposium (SPMB), pp. 1-6. 2011.



- [14] M. Egmont-Petersen, D. de Ridder, and H. Handels. Image processing with neural networks—a review. *Pattern recognition*, 35(10), pp. 2279-2301. 2002.
- [15] N. K. Ragesh, A. R. Anil, & R. Rajesh. Digital image denoising in medical ultrasound images: a survey. In *ICGST AIML 11th Conference*, Dubai, UAE, 12, pp. 67 - 73. 2011.
- [16] M. Yasmin, M. Sharif, and S. Mohsin. Neural networks in medical imaging applications: A survey. *World Applied Sciences Journal*, 22(1), pp. 85-96. 2013.
- [17] A. Chaudhry, A. Khan, J. Y. Kim, and Q. Q. Niu. Intelligent Image Restoration Approach: Using Neural Networks to Eradicate Dilemma in Punctual Kriging. *Life Science Journal*, 10(1), pp. 1631-1641. 2013.
- [18] R. H. Pugmire, R. M. Hodgson, and R.I. Chaplin. The properties and training of a neural network based universal window filter developed for image processing tasks. In S. Amari, N. Kasabov (Eds.), *Brain-like computing and intelligent information systems*, Springer-Verlag, Singapore, pp. 49–77. 1998.
- [19] A. Chaudhry, A. Khan, A. M. Mirza, A. Ali, M. Hassan, and J. Y. Kim. Neuro fuzzy and punctual kriging based filter for image restoration. *Applied Soft Computing*, 13(2), pp. 817-832. 2013.
- [20] A. J. Schofield, P. A. Mehta, T. J. Stonham. A system for counting people in video images using neural networks to identify the background scene, *Pattern Recognition*, 29 (8), pp. 1421–1428. 1996.
- [21] R. Sammouda, J. A. Hassan, M. Sammouda, A. Al-Zuhairy, H. A. ElAbbas, *Computer Aided Diagnosis System for Early Detection of Lung Cancer Using Chest Computer Tomography Images*. In *ICGST GVIP 5th Conference*, Cairo, Egypt, pp. 1 - 8. 2005.
- [22] M.H. Jafari, E. Nasr-Esfahani, N. Karimi, S. M. Soroushmehr, S. Samavi, & K. Najarian. Extraction of Skin Lesions from Non-Dermoscopic Images Using Deep Learning, *arXiv preprint arXiv:1609.02374*. 2016
- [23] F. Amato, A. López, E. M. Peña-Méndez, P. Vañhara, A. Hampl, and J. Havel. Artificial neural networks in medical diagnosis. *Journal of applied biomedicine*, 11(2), pp. 47-58. 2013.
- [24] K. Korotov and R. Garcia. Computerized analysis of pigmented skin lesions: a review. 2012.
- [25] G. Zhang, B. E. Patuwo, and M. Y. Hu. Forecasting with artificial neural networks: The state of the art. *International journal of forecasting*, 14(1), pp. 35-62. 1998.
- [26] N. Karayiannis, and A. N. Venetsanopoulos. *Artificial neural networks: learning algorithms, performance evaluation, and applications*. Springer Science & Business Media, 209. 2013.
- [27] W. S. McCulloch, and W. Pitts. A logical calculus of the ideas immanent in nervous activity. *The bulletin of mathematical biophysics*, 5(4), pp. 115-133. 1943.
- [28] I. A. Basheer, and M. Hajmeer. Artificial neural networks: fundamentals, computing, design, and application. *Journal of microbiological methods*, 43(1), pp. 3-31. 2000.
- [29] B. Müller, J. Reinhardt, and M. T. Strickland. *Neural networks: an introduction*. Springer Science & Business Media. 2012.
- [30] G. Deco, and D. Obradovic. *An information-theoretic approach to neural computing*. Springer Science & Business Media. 2012.
- [31] F. Wang, V. K. Devabhaktuni, C. Xi, and Q. J. Zhang. Neural network structures and training algorithms for RF and microwave applications. *International Journal of RF and Microwave Computer-Aided Engineering*, 9(3), pp. 216-240. 1999.
- [32] T. Fawcett. ROC graphs: Notes and practical considerations for researchers. In *Machine learning Journal*, 31(1), pp. 1-38. 2004.
- [33] K. H. Zou, A. J. O'Malley, and L. Mauri. Receiver-operating characteristic analysis for evaluating diagnostic tests and predictive models. *Circulation*, 115(5), pp. 654-657. 2007.

Biographies



Géraud Azehou-Pazou received his Engineer degree in Informatics and Telecommunications in 2012 and the DEA degree “Diplôme d’Etudes Approfondies” in 2013 from the Polytechnic School of Abomey-Calavi, Benin. Currently he is a PhD student at University of Abomey-Calavi in the LETIA

Laboratory under the supervision of Kokou Assogba. His research interests include Image processing, Artificial Intelligence, Object detection and tracking.



Dr. Kokou Assogba obtained his PhD degree in Images and Signal Processing in 1999 at University Paris XII Val de Marne, France. He is working, since as teacher-researcher in Computer Science and Electronics at University of Abomey-Calavi. He is Senior

Member and recently became Head of the Laboratory of Electronics, Telecommunications and Applied Informatics (LETIA). His main research interests are: Digital Image processing, Pattern Recognition, Images Segmentation and smart technology.







Robust Color Image Watermarking Technique Using DWT and Homomorphic based SVD

Khalid A. Al-Afandy¹, EL-Sayed M. EL-Rabaie², Fathi E. Abd El-Samie², Osama S. Faragallah¹, Ahmed ELmhalaway¹, A. M. Shehata¹

1. Menoufia University, Faculty of Electronic Engineering, Computer Engineering and Science Department.
2. Menoufia University, Faculty of Electronic Engineering, Electronic and Communication Department

Abstract

This paper presents a robust hybrid image watermarking technique using Discrete Wavelet Transform (DWT) and Singular Value Decomposition (SVD). The DWT is utilized to divide the image into non-overlapping bands. The reflectance component of the low-frequency sub-band (LL) is extracted using homomorphic transform for each color (red, green, and blue). The watermark embedding is performed using SVD on the reflectance component of the LL sub-band. The results of the proposed watermarking technique are compared with some state-of-the-art techniques. The comparison test is performed on images with different resolutions. It is based on visualization to detect any degradations in the watermarked image, Peak Signal-to-Noise Ratio (PSNR) of watermarked image, and Normalized Correlation (NC) of extracted watermark.

Keywords: Watermarking, Discrete Wavelet Transform (DWT), Discrete Cosine Transform (DCT), Singular Value Decomposition (SVD), Homomorphic transform.

Nomenclature

DWT	Discrete Wavelet Transform
DCT	Discrete Cosine Transform
SVD	Singular Value Decomposition
MSE	Mean Squared Error
PSNR	Peak Signal to Noise Ratio
NC	Normalized Correlation

1. Introduction

In recent years, information technology, digital data, and multimedia have been easily duplicated, manipulated, and distributed. So, it is very important to have copyright protection to save owners copyrights. There are several protection techniques, one of them is watermarking. Watermarking technology is the process of hiding an image called watermark or label into original digital data (image, video or audio) [1]. Watermarked images must be robust enough to survive attacks [1]. Watermarking techniques can be classified into two categories; spatial domain and transform domain [1]. Several techniques of

transform domain watermarking are discussed in this paper.

One of these techniques is the DWT [3,5,9]. It is based on dividing the image into four non-overlapping bands; approximation sub-band (LL), horizontal sub-band (LH), vertical sub-band (HL), and diagonal sub-band (HH) [3,5,6,9].

Another widely-used technique of transform domain watermarking is the Discrete Cosine Transform (DCT) [11-16]. This transform is used to convert spatial domain image into discrete transform domain [14]. Another widely-used technique of transform domain watermarking is SVD [10,11]. It is an effective numerical analysis tool used to analyze matrices. The SVD transformation divides the matrix into three matrices with the same size of the original matrix; two orthogonal matrices and one diagonal matrix [9]. Then, the watermark is embedded in the diagonal matrix [6,8-10,16-18].

Another domain used for watermarking is the homomorphic domain [9]. It is based on image intensity represented as light illumination and reflectance of the image. Illumination is approximately constant and reflectance is variable from image to image. Thus, the reflectance of the image is used to perform the watermarking process. It must be noted that the SVD technique is utilized for avoiding the redundancy resulting from the existence of two components of the image in the homomorphic domain [9].

Hybrid techniques are widely used for watermarking. This can be accomplished by combining two or more techniques to achieve better results.

One of these hybrid techniques is the DCT-DWT [14]. It is based on dividing the RGB color image into three matrices (red, green and blue). The DCT is implemented on each color. Watermark embedding is performed on the LL sub-band by utilizing the DWT to divide the DCT domain into four sub-bands for each color [14-16].

Another hybrid technique is the DWT-SVD [2]. It is based on utilizing the DWT to divide the image into four sub-bands. The LL sub-band is divided into three matrices (red, green and blue). Watermark embedding is performed by



applying the SVD on each color of the LL sub-band [2,6,9,18].

The main aim of this paper is presenting a hybrid technique to achieve robust watermarking based on [1]. The rest of this paper is organized as follows. Section 2 gives a literature review. The evaluation metrics are shown in section 3. Section 4 discusses the proposed technique. The simulation results are illustrated in section 5. Section 6 presents the conclusions followed by the more relevant references.

2. Literature Review

Surveying the literature there are three main techniques most commonly used in color image watermarking: Discrete Wavelet Transform (DWT) [3-5,9], Discrete Cosine Transform (DCT) [6,9,12,15] and Singular Value Decomposition (SVD) [8-10,17]. Hybrid techniques are widely used in watermarking. There are two main hybrid techniques most commonly used DCT-DWT [7,13-15] and DWT-SVD [2]. This paper is the extended paper from conference paper [1].

Discrete Wavelet Transform (DWT)

Wavelet transform is an information processing method; it has been widely used in many fields including image processing. The DWT divide an image into four non-overlapping bands. These bands are calculated in different frequencies [9]. Figure 1 shows the four sub-bands; approximation sub-band (low frequency LL), horizontal sub-band (high frequency LH), vertical sub-band (high frequency HL), and diagonal sub band (high frequency HH). Figure 2 show the low pass and high pass analysis filter $h[-m]$, $g[-m]$ [3-5,9].

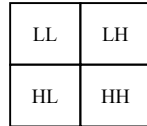


Figure 1. The DWT sub-bands.

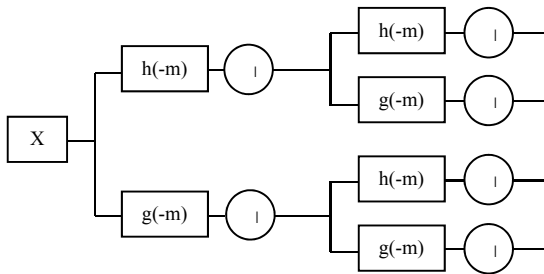


Figure 2. Two dimensional decomposition using the DWT.

Discrete Cosine Transform (DCT)

Discrete Cosine Transform (DCT) is a standout amongst the most well known orthogonal change strategies utilized as a part of picture preparing. High vitality compaction property of DCT is the reason. In watermarking, this property helps in choosing the area in picture to insert the watermark with most robustness [6]. DCT divides aircraft carrier signal into three frequencies bands namely low, middle, and heights frequency bands. It is frequency orbit

watermarking technique as watermark is embedded into one of these three bands, carrier signal pixel are not modified directly [12].

Two dimension discrete cosine transform 2D-DCT is defined as [7]

$$F(jk) = a(j)a(k) \sum_{m=0}^{M-1} \sum_{n=0}^{N-1} f(m,n) \cos \left[\frac{(2m+1)j\pi}{2M} \right] \cos \left[\frac{(2n+1)k\pi}{2N} \right] \quad (1)$$

Inverse transform 2D-IDCT is defined as [7]

$$f(mn) = \sum_{j=0}^{M-1} \sum_{k=0}^{N-1} a(j)a(k)F(jk) \cos \left[\frac{(2m+1)j\pi}{2M} \right] \cos \left[\frac{(2n+1)k\pi}{2N} \right] \quad (2)$$

Where $0 \leq j \leq M-1$, $0 \leq k \leq N-1$,

$$a(j) = \begin{cases} \frac{1}{\sqrt{M}}, & j = 0 \\ \sqrt{\frac{2}{M}}, & 1 \leq j \leq M-1 \end{cases} \quad \text{and} \quad a(k) = \begin{cases} \frac{1}{\sqrt{N}}, & k = 0 \\ \sqrt{\frac{2}{N}}, & 1 \leq k \leq N-1 \end{cases}$$

Singular Value Decomposition (SVD)

SVD is an effective numerical analysis tool used to analyze matrices. The SVD transformation matrix divides the matrix into three matrices with the same size of the original matrix. Then SVD of A is defined as:

$$A = USV^T \quad (3)$$

Where U and V are orthogonal matrices and S is a diagonal matrix. The entries in these diagonal matrices are called singular value of the matrix A. Applying this technique in RGB color images requires image color separation into three matrices red, green and blue. Implement the SVD watermarking in each matrix and finally reconnect these three matrices given the final watermarked color image [9]. For embedding a watermark into host image, the SVD is performed onto the host image as in (3). The watermark is added to the S matrix of the original matrix as:

$$D = S + kW \quad (4)$$

SVD performed as a new matrix:

$$D = U_w S_w V_w^T \quad (5)$$

The watermarked image is:

$$A_w = US_w V^T \quad (6)$$

For extract watermark the watermarked image is:

$$A_w^* = U^* S_w^* V^{*T} \quad (7)$$

The matrix include watermark is computed:

$$D^* = U_w S_w^* V_w^{*T} \quad (8)$$

It's possible to corrupt watermark [6,8,9,17,18]

$$W^* = (D^* - S) / k \quad (9)$$

The hybrid technique (DCT-DWT)

The hybrid technique DCT-DWT is based on utilized the DWT to divide DCT domain into four sub-bands [14]. The RGB color image is divided into three matrices (red, green and blue). The DCT domain is extracted by applying the DCT for each color. Embedding watermark is done on sub-band LL by utilize DWT to divide the DCT domain into four sub-bands for each color [14-16].

The hybrid technique (DWT-SVD)

The hybrid technique DWT-SVD is based on utilized the DWT to divide image into four sub-bands and then applying SVD into diagonal sub-band (LL) [2]. The DWT is utilized to divide image into four sub-bands. The sub-band LL is divided into three matrices (red, green and blue). Embedding watermark is done by applying SVD for each color of sub-band LL [2,6,9,18].



3. Evaluation Matrices

All tests were performed using an Intel® core™i5 CPU M450 @2.4GHz with 6GB Memory and running Windows 7 64-bit operating system and using MATLAB 8. All the images used are 512×512 colored JPEG images. There are five main tests to determine the performance of a watermarking technique. Visually test to determine the invisibility of watermark and any degradation in quality or colors in the watermarked image compared to original image. The Peak Signal-to-Noise Ratio (PSNR) of the watermarked image and the Normalization Correlation (NC) for the extracted watermark are calculated. Applying attacks on the watermarked image then extracting the watermark and repeating the NC tests again after attacks. Calculate the CPU time for embedding algorithm.

PSNR can be calculated by [9]

$$MSE = \frac{1}{M \times N} \sum_{x=0, y=0}^{M-1, N-1} (A_w(x, y) - A(x, y))^2 \quad (10)$$

$$PSNR (DB) = 10 \log_{10} \frac{255^2}{MSE} \quad (11)$$

where A is original image, A_w is watermarked image and M, N size of original and watermarked image. NC calculate given by [9]

$$NC = \frac{W^* \cdot W}{\|W^*\| \cdot \|W\|} \quad (12)$$

where W is original watermark and W^* is extract watermark.

4. The Proposed Watermarking Technique

The proposed technique presented here is DWT-homomorphic based SVD. The DWT is utilized to divide image into four non-overlapping bands. The reflectance components of the sub-band LL is extracted using homomorphic transform for each color (red, green and blue). Embedding watermark is done by applying the SVD on reflectance components of the sub-band LL. The sub-band (LL) intensity can be represented as:

$$f_{LL}(n_1, n_2) = i(n_1, n_2) r(n_1, n_2) \quad (13)$$

where $i(n_1, n_2)$ is the light illumination and $r(n_1, n_2)$ is the reflectance of the object to be sub-band imaged. The homomorphic transform is performed.

$$\ln [f_{LL}(n_1, n_2)] = \ln [i(n_1, n_2)] + \ln [r(n_1, n_2)] \quad (14)$$

The LPF and the HPF are applied to $\log [f_{LL}(n_1, n_2)]$ to separate the illumination component I and the reflectance component R , respectively, for each pixel value in the form of matrices. The SVD is performed on the (R matrix).

$$R = USV^T \quad (15)$$

The watermark (W matrix) is added to the SVs of the reflectance matrix.

$$D = S + kW \quad (16)$$

The SVD is performed on the new modified matrix (D matrix).

$$D = U_w S_w V_w^T \quad (17)$$

The sub-image (R_w matrix) is obtained by using the modified matrix (S_w matrix)

$$R_w = U S_w V^T \quad (18)$$

An inverse homomorphic transform is performed on I and R_w to obtain a matrix X_w

$$X_w = R_w + I \quad (19)$$

The sub-band (LL) of watermarked image can be obtained as

$$f_{LL_w} = \exp (X_w) \quad (20)$$

So watermarked image can be obtained by reconnect colors (Red, Green, Blue) then applying the inverse DWT to produce watermarked image F_w .

To extract the possibly corrupted watermark from the possibly distorted watermarked image, given U, S_w, V matrices and the possibly distorted sub-image F_w , the above steps are reversed as follows:

The homomorphic transform is performed on the sub-band (LL) for watermarked image f_{LL_w}

The HPF is used to get the possibly corrupted reflectance component R_w^* .

The SVD is performed on the R_w^* matrix.

$$R_w^* = U^* S_w^* V^{*T} \quad (21)$$

The matrix that includes the watermark is computed.

$$D^* = U_w S_w^* V_w^{*T} \quad (22)$$

The possibly corrupted watermark is obtained.

$$W^* = (D^* - S) / k \quad (23)$$

The proposed technique's embedding algorithm is shown in figure 3 and extracting algorithm is shown in figure 4.

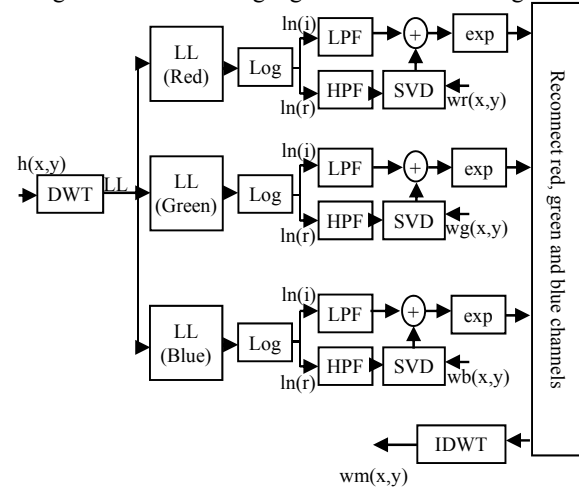


Figure 3. The embedding algorithm.

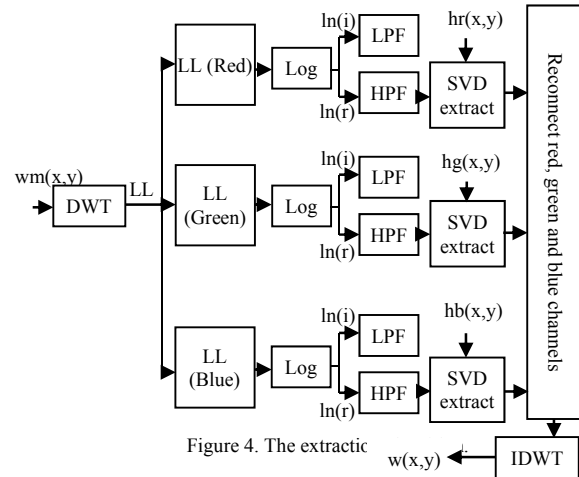


Figure 4. The extracting

5. Simulation Results

There are two experiments for each technique one using RGB color JPEG images with size 512×512, resolution 72×72 dpi and bit depth 24 host image pepper and watermark fruits, and the other test using RGB color JPEG images with size 512×512, resolution 180×180 dpi and bit depth 24 host image Khalid and watermark Rokayya as shown in figure 5 where (a) host image pepper, (b) watermark image fruits, (c) host image Khalid and (d) watermark image Rokayya. Visualization test results for



proposed technique compared with the other state of art techniques that stated in literature review without attacks are shown in figure 6. Figure 7 shows the rotate 30° attacks. Rotate 45° attacks are shown in figure 8. Figure 9 shows the rotate 60° attacks. Gaussian noise attacks with variance parameter 0.01 are shown in figure 10. Figure 11 shows the Gaussian noise attacks with variance parameter 0.05. Gaussian noise attacks with variance parameter 0.1 are shown in figure 12. Figure 13 shows the resize to 256×256 attacks then resize to 512×512 . Motion blur attacks are shown in figure 14. Figure 15 shows the disk blur attacks. Average blur attacks are shown in figure 16, Figure 17 shows the JPEG compression 20% attacks. JPEG compression 40% attacks are shown in figure 18. Figure 19 shows the JPEG compression 60% attacks. Crop attacks are shown in figure 20. Table 1 and table 2 shows the evaluation matrices results (PSNR and NC) without attacks and algorithm CPU time for the proposed technique compared with the other state of art techniques. The NC for extracted watermark after attacks for the proposed technique compared with the other state of art techniques shown in figure 21 and figure 22.



Figure 5. (a) host image pepper, (b) watermark fruits, (c) host image Khalid, (d) watermark Rokaya.

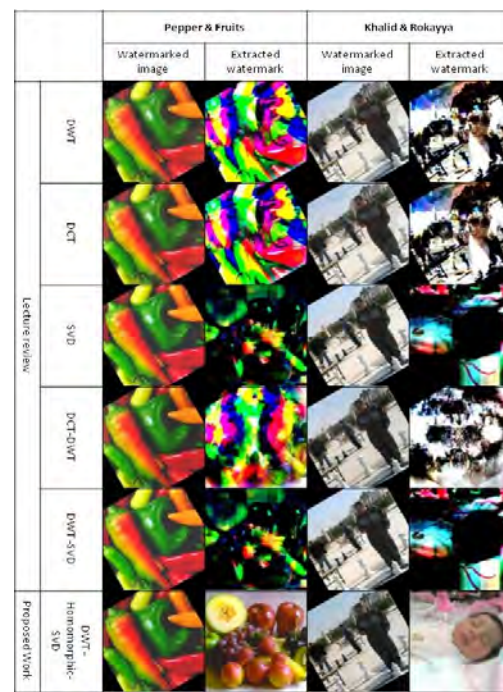


Figure 7. Visualization tests after rotate 30° attacks.

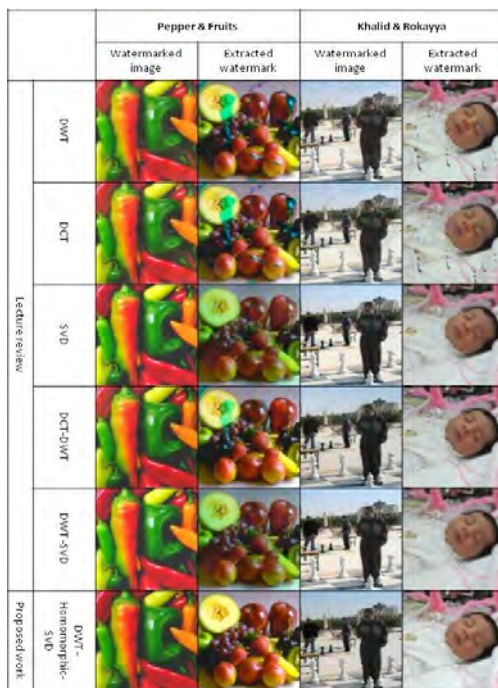


Figure 6. Visualization tests without any attacks.

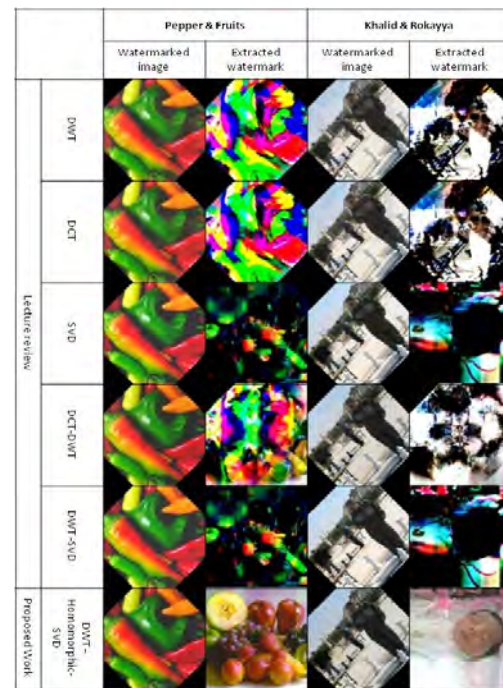


Figure 8. Visualization tests after rotate 45° attacks.



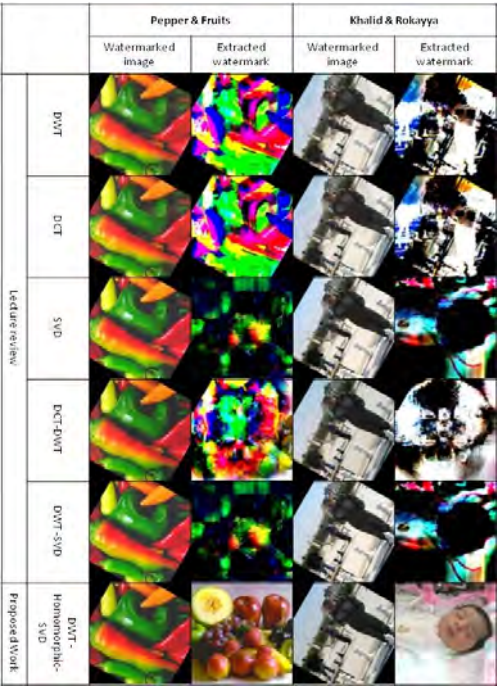


Figure 9. Visualization tests after rotate 60° attacks.

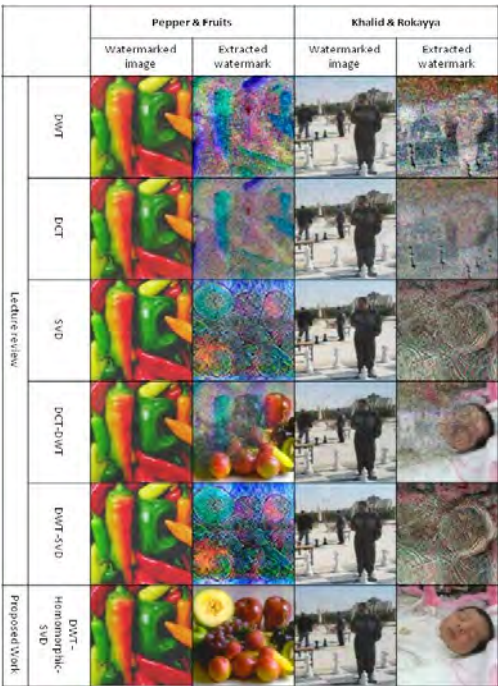


Figure 11. Visualization tests after Gaussian noise attacks with variance parameter 0.05.

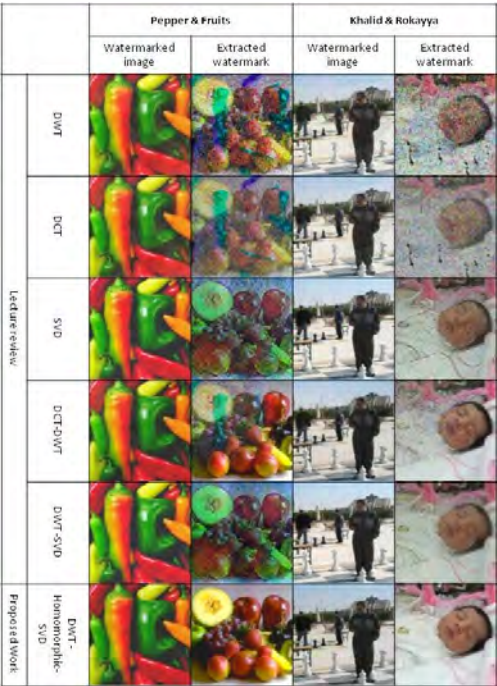


Figure 10. Visualization tests after Gaussian noise attacks with variance parameter 0.01.

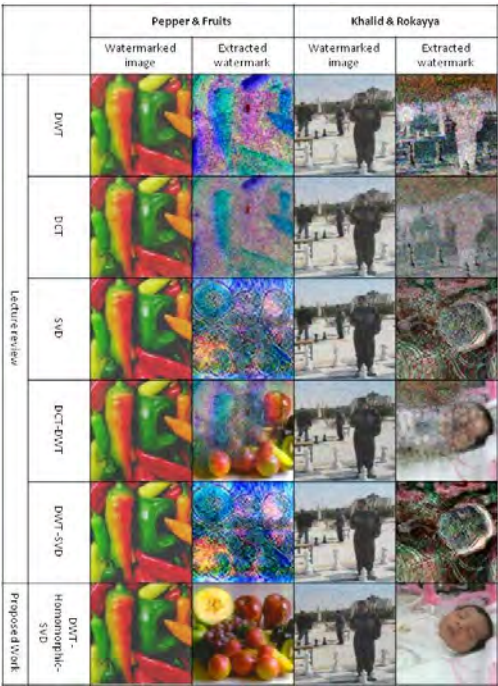


Figure 12. Visualization tests after Gaussian noise attacks with variance parameter 0.1.



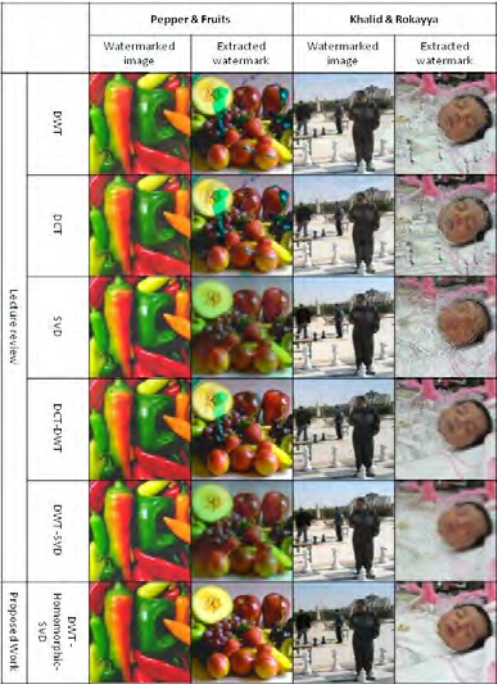


Figure 13. Visualization tests after resize to 256×256 then resize to 512×512 attacks.

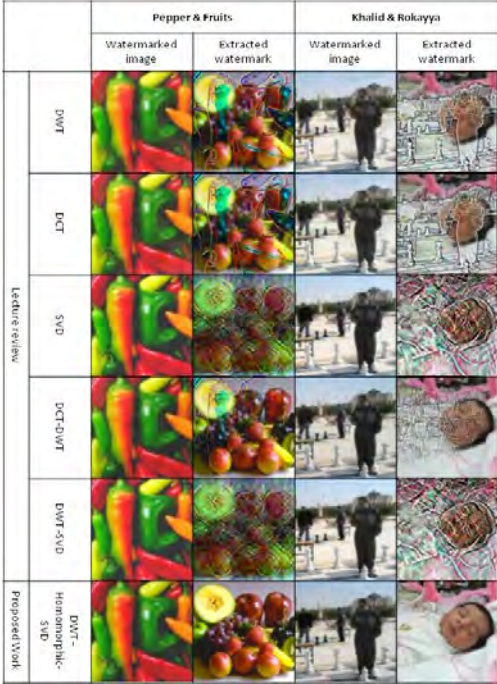


Figure 15. Visualization tests after disk blur attacks.

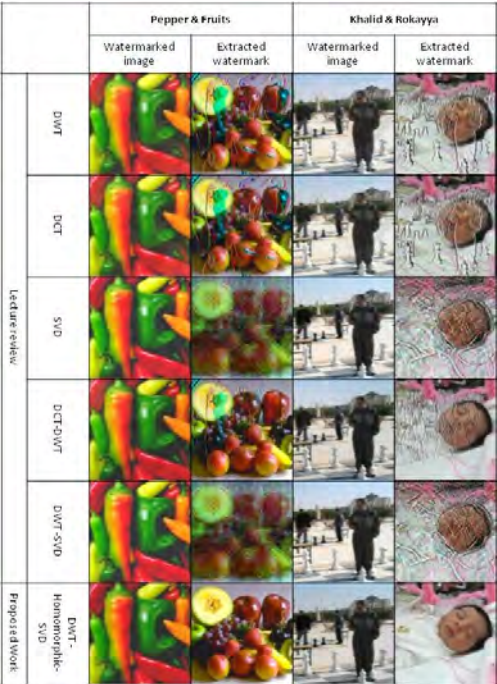


Figure 14. Visualization tests after motion blur attacks.

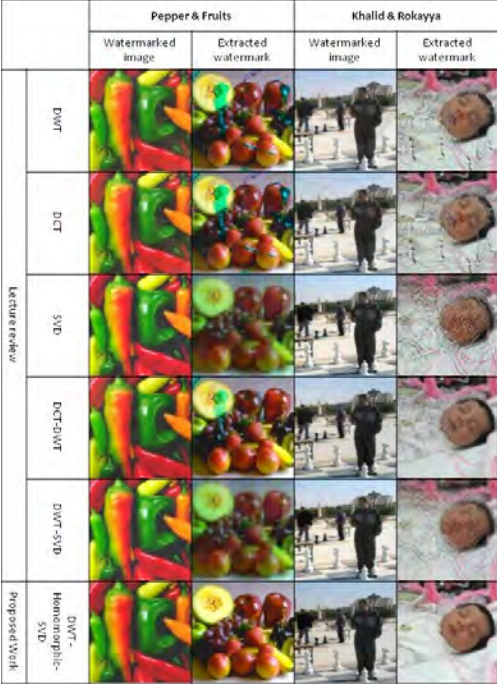


Figure 16. Visualization tests after average blur attacks.























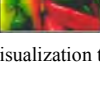



		Pepper & Fruits		Khalid & Rokayya	
		Watermarked image	Extracted watermark	Watermarked image	Extracted watermark
Lecture review	DWT				
	DCT				
	SVD				
	DCT-DWT				
	DWT-SVD				
	Proposed Work				

Figure 17. Visualization tests after JPEG compression 20% attacks.





















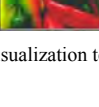



		Pepper & Fruits		Khalid & Rokayya	
		Watermarked image	Extracted watermark	Watermarked image	Extracted watermark
Lecture review	DWT				
	DCT				
	SVD				
	DCT-DWT				
	DWT-SVD				
	Proposed Work				

Figure 19. Visualization tests after JPEG compression 60% attacks.





















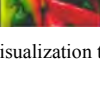



		Pepper & Fruits		Khalid & Rokayya	
		Watermarked image	Extracted watermark	Watermarked image	Extracted watermark
Lecture review	DWT				
	DCT				
	SVD				
	DCT-DWT				
	DWT-SVD				
	Proposed Work				

Figure 18. Visualization tests after JPEG compression 40% attacks.






















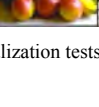
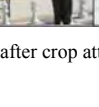

		Pepper & Fruits		Khalid & Rokayya	
		Watermarked image	Extracted watermark	Watermarked image	Extracted watermark
Lecture review	DWT				
	DCT				
	SVD				
	DCT-DWT				
	DWT-SVD				
	Proposed Work				

Figure 20. Visualization tests after crop attacks.



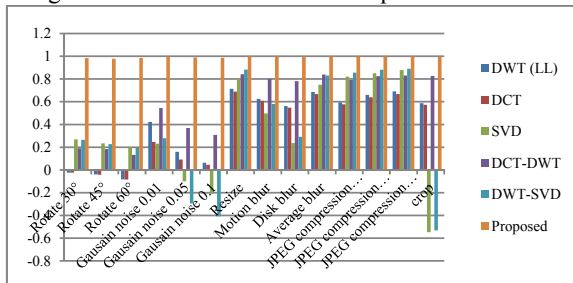
Table 1. The proposed watermarking technique compared with other state of arts techniques based on PSNR for watermarked image, NC for extracted watermark without attacks and CPU time for embedding algorithm for pepper and fruits images.

	DWT	DCT	SVD	DCT-DWT	DWT-SVD	Proposed
PSNR red	24.716	24.727	25.615	28.969	25.620	35.856
PSNR green	25.826	25.838	26.176	29.284	26.187	38.479
PSNR blue	27.676	27.688	28.222	31.376	28.229	34.896
NC red	0.7316	0.7107	0.9115	0.5896	0.9124	0.9963
NC green	0.9673	0.9364	0.9924	0.9785	0.9943	0.9980
NC blue	0.9145	0.8861	0.9594	0.9541	0.9634	0.9945
CPU time	1.4040	0.8424	3.8844	1.0140	2.5584	3.1044

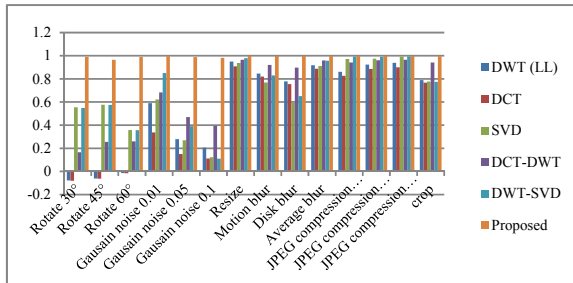
Table 2. The proposed watermarking technique compared with other state of arts techniques based on PSNR for watermarked image, NC for extracted watermark without attacks and CPU time for embedding algorithm for Khalid and Rokayya images.

	DWT	DCT	SVD	DCT-DWT	DWT-SVD	Proposed
PSNR red	22.902	22.919	22.944	28.234	22.939	33.301
PSNR green	23.322	23.344	23.388	29.011	23.391	33.793
PSNR blue	23.304	23.331	23.324	28.618	23.325	32.737
NC red	0.8876	0.7207	0.9955	0.8942	0.9954	0.9976
NC green	0.9394	0.7870	0.9980	0.9267	0.9980	0.9987
NC blue	0.9025	0.7742	0.9978	0.9219	0.9978	0.9985
CPU time	1.5288	0.7956	3.8064	1.0296	2.8236	3.1200

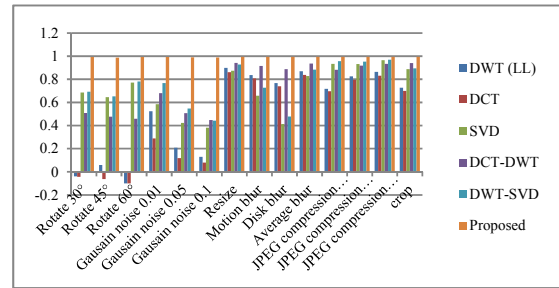
As shown from visualization test and experimental results, by visual inspection, the results reveal that no noticeable variations exist between the watermarked and the original images which enforce the fidelity of the proposed watermarking technique. The watermarked images and the extracted watermarks for the proposed watermarking technique have a high PSNR, NC respectively compared with the other state of art techniques in the three color channels. The embedding algorithm CPU time for the proposed technique is higher with few seconds than the other hybrid techniques but it is little speed than the SVD techniques. So the CPU time for the proposed technique is in range of the other state of art techniques.



(a) NC for extracted watermark images for red channels after attacks

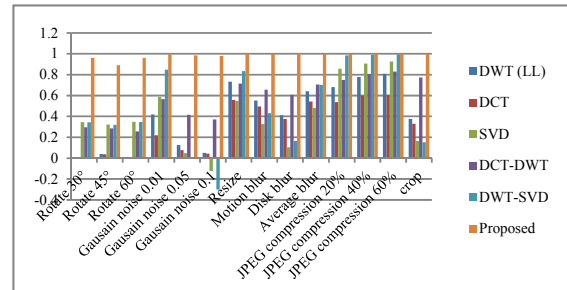


(b) NC for extracted watermark images for green channels after attacks

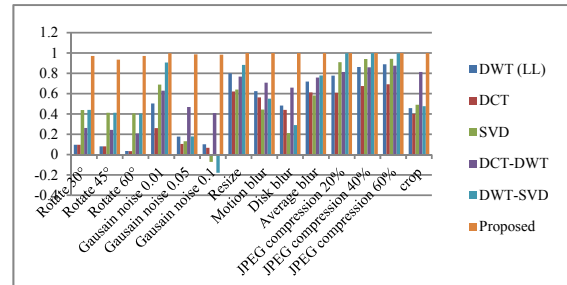


(c) NC for extracted watermark images for blue channels after attacks

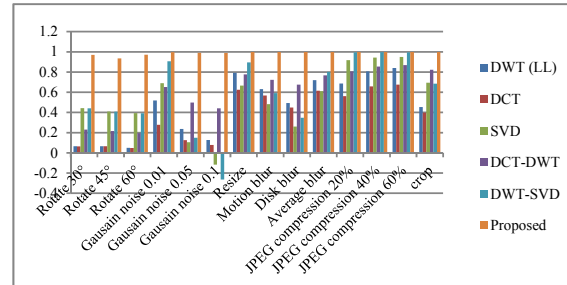
Figure 21. The proposed watermarking technique compared with other state of arts techniques for pepper and fruits images based on NC for extracted watermark after attacks



(a) NC for extracted watermark images for red channels after attacks



(b) NC for extracted watermark images for green channels after attacks



(c) NC for extracted watermark images for blue channels after attacks

Figure 22. The proposed watermarking technique compared with other state of arts techniques for Khalid and Rokayya images based on PSNR for watermarked image, NC for extracted watermark after attacks

As shown from visualization test, experimental results and evaluation figures after attacks, results illustrate that the extracted watermarks for the proposed watermarking technique have a high NC compared with the other state of art techniques in the three color channels, which guarantees watermarking existence. The NC for the extracted watermarks for the proposed technique is higher compared with the other state of art techniques in the three color channels. It means that the proposed technique is more robust against attacks.



6. Conclusions

This paper proposes an image watermarking hybrid technique using the DWT-homomorphic based SVD technique. It embeds the watermark during applying the SVD on the reflectance components of the sub-band LL by utilizing the DWT to divide the image into non-overlapping bands. The reflectance components of the sub-band LL is extracted using the homomorphic transform for each color (red, green and blue). It is shown that we can embed an RGB color image watermark to an RGB color host image with the same size. The experimental results demonstrated that the DWT-homomorphic based SVD watermarking has a high fidelity and robustness in the presence of different types of attacks. There is always a large probability for watermark detection. The embedding algorithm CPU time is in range of the other hybrid techniques. The achieved results also reveal the superiority of the proposed DWT-homomorphic based SVD watermarking technique over other state of art watermarking techniques.

7. References

- [1] Khalid. A. Al-Afandy, El-Sayed M. EL-Rabaie, Fathi E. Abd El-Samie, Osama. S. Faragallah, and Ahmed ELmhalawy, "Efficient Color Image Watermarking Using Homomorphic Based SVD in DWT Domain", 2016 Fourth International Japan-Egypt Conference on Electronics, Communications and Computers (JEC-ECC), IEEE, PP. 43-47, 2016.
- [2] Bhatnagar, Gaurav, and Balasubramanian Raman, "A New Robust Reference Watermarking Scheme Based on DWT-SVD", Computer Standards & Interfaces, Vol. 3, No. 5, PP. 1002-1013, 2009.
- [3] Giri, Kaiser J., Mushtaq Ahmad Peer, and P. Nagabhushan, "A Robust Color Image Watermarking Scheme Using Discrete Wavelet Transformation", International Journal of Image, Graphics and Signal Processing (IJIGSP), Vol. 7, No.1, PP. 47-52, 2014.
- [4] Saini, Mandeep Singh, B. Venkata Kranthi, and Gursharanjeet Singh Kalra, "Comparative Analysis of Digital Image Watermarking Techniques in Frequency Domain Using MATLAB SIMULINK", International Journal of Engineering Research and Applications (IJERA) ISSN, Vol. 2, No. 4, PP. 2248-9622, 2012.
- [5] Ganjir, Neha, and Nivedita Singh, "Bi-Orthogonal Wavelet Transform Based 3-D Image Watermarking on Colour Image", International Journal of Computer Science and Mobile Computing, Vol. 3, No. 8, PP. 451-456, 2014.
- [6] Kekre, Dr HB, Dr Tanuja Sarode, and Shachi Natu, "Hybrid Watermarking of Colour Images Using DCT-Wavelet, DCT and SVD", International Journal of Advances in Engineering and Technology, Vol. 6, No. 2, PP. 769-779, 2013.
- [7] Jiansheng, Mei, Li Sukang, and Tan Xiaomei, "A Digital Watermarking Algorithm Based on DCT and DWT", International Symposium on Web Information Systems and Applications (WISA'09), Vol. 9, No. 1, PP. 104-107, 2009.
- [8] Narasimhulu, C. Venkata, and K. Satya Prasad, "A New SVD Based Hybrid Color Image Watermarking for Copyright Protection Using Contourlet Transform", International journal of computer applications, Vol. 20, No.8, PP. 18-27, 2011.
- [9] Hanaa Abdalaziz, "Data Hiding and applications", Ph.D. Thesis, Department of Electronics and Communication Engineering, Faculty of Engineering, Zagazig University, 2011.
- [10] Sheriff, Sura Ramzi, "Digital Image Watermarking Using Singular Value Decomposition", Third Scientific Conference Information Technology, Vol. 7, No. 3, PP. 187-199, 2010.
- [11] Ji, Ke, et al., "A DCT And SVD Based Watermarking Technique To Identify Tag", arXiv preprint arXiv:1502.02969, 2015.
- [12] Bhaskar, T., and D. Vasumathi., "DCT Based Watermark Embedding into Mid Frequency of DCT Coefficients Using Luminance Component", International Research Journal of Engineering and Technology (IRJET), Vol. 2, No. 3, PP. 738-741, 2015.
- [13] Saini, Lalit Kumar, and Vishal Shrivastava., "Analysis of Attacks on Hybrid DWT-DCT Algorithm for Digital Image Watermarking With MATLAB", arXiv preprint arXiv:1407.4738, Vol. 2, No. 3, PP. 123-126, 2014.
- [14] Mukherjee, Parneli, and Saurabh Mitra., "A Review on Copy-Move Forgery Detection Techniques Based on DCT and DWT", International Journal of Computer Science and Mobile Computing, Vol. 4, No. 3, PP. 702-708, 2015.
- [15] Benoraira, Ali, Khier Benmahammed, and Noureddine Boucenna., "Blind Image Watermarking Technique Based on Differential Embedding in DWT and DCT Domains", EURASIP Journal on Advances in Signal Processing, Vol. 2015, No.1, PP 1-11, 2015.
- [16] Kaur, Ramandeep, and Jatinder Kumar., "Integrated DCT, DWT and Modified SVD Based Digital Image Watermarking", International Journal of Computer Science and Mobile Computing, Vol. 4, No. 5, PP. 1002-1011, 2015.
- [17] Moulick, Subhayan Roy, et al., "Reliable SVD Based Semi-Blind and Invisible Watermarking Schemes", arXiv preprint arXiv:1503.01934, 2015.
- [18] Rahman, Md Atiqur, and MM Fazle Rabbi., "DWT-SVD Based New Watermarking Idea in RGB Color Space", International Journal of Signal Processing, Image Processing and Pattern Recognition, Vol. 8, No.6, PP. 193-198, 2015.



Biographies



Khalid A. Al-Afandy received his B.Sc. from 1993 at 1997 Currently he is working for Town Gas and he is a Master student at Menoufia University Faculty of Electronic Engineering in the Image Watermarking under the supervision of Prof. EL-Sayed M. EL-Rabaie.



Dr. Osama S. Faragallah is currently Associate Professor at Menoufia University Faculty of Electronics Engineering, in the Department of Computer Science and Engineering. He is a coauthor of about 100 papers in international journals and conference proceedings, and two textbooks.



Prof. EL-Sayed M. EL-Rabaie is currently Professor at Menoufia University Faculty of Electronics Engineering, in the Department of Electronic and Communication. He is the Editorial Board for several scientific journals.



Dr. Ahmed M. Elmalahawy is currently Associate Professor at Menoufia University Faculty of Electronics Engineering, in the Department of Computer Science and Engineering. His interest is in artificial Intelligence mainly Agent technology and multi Agent System and machine learning. He had many publications in these fields.



Prof. Fathi E. Abd EL-Samie is currently Professor at Menoufia University Faculty of Electronics Engineering, in the Department of Electronic and Communication.



Dr. Ahmed M. Shehata is currently Teaching Staff Member at Menoufia University Faculty of Electronics Engineering, in the Department of Computer Science and Engineering.





Region Based Integrated Approach for Image Retrieval

¹TALLURI. SUNIL KUMAR, ²T.V.RAJINIKANTH · ³B. ESWARA REDDY

¹VNR Vignana Jyothi Institute of Engineering and Technology, Hyderabad, Telangana, India

²SNIST, Hyderabad, Telangana India.

³Professor in CSE and Principal, JNTU-A College of Engineering, Kalikiri, Chittoor Dist, Andhra. Pradesh, India.

Email: ¹sunilkumart1973@gmail.com, ²rajinitv@gmail.com, ³eswarcejntua@gmail.com,

Abstract

This paper proposes an integrated method for efficient content based image retrieval using color, shape and rotational invariant texture features. The present paper derived rotational invariant features on each region. To derive shape features textons are computed. To represent texture features gray level co-occurrence matrix (GLCM) features are derived on region based rotational invariant texton matrix. These features are combined with HSV histograms. The advantage of region based models is they are more applicable when working with images of large size and especially in real time environment. The image retrieval is performed on five categories of Wang database and the present method is compared with texton co-occurrence matrix (TCM), color correlogram gradient (CCG) and GLCM methods.

Keywords: GLCM, HSV; shape; texture; rotation invariant features;

1. Introduction

These days there is a huge expansion on browsing of the digital libraries or databases. Searching and retrieving images from these libraries has become a crucial and tedious task for human annotation and this has created the dire need of content based image retrieval (CBIR) methods. The CBIR methods are capable of retrieving the desired images from these libraries based on the image contents. The CBIR models makes use of visual contents of an image like color, shape, texture mosaic, faces and spatial layouts for efficient image retrieval (IR). It is highly impossible to represent an image with a single best feature and it is due to the fact that user may capture photographs from different angles, lighting conditions, reflection etc. The traditional image retrieval (IR) methods are text based methods. The images are retrieved by matching the corresponding index text or meta-data associated with images. A comprehensive literature survey on CBIR is presented in [1-4].

The color content of an image is one of the powerful descriptor of CBIR and it can keep semantically intact

and it is robust to noise, change in size, image degradation and orientation. There are various CBIR systems that are based on color descriptors [5, 6, 7, 8]. The retrieval performance of these degrades on huge databases due to color shading problems. One of the most visual characteristic feature of the image is the texture and texture features plays an important and crucial role in many applications like image classification [9, 10, 11], face recognition [12, 13], smoke detection [14], age and facial expressions identification [15, 16], pedestrian detection [17, 18] and image retrieval [19, 20, 21, 22, 23]. Various methods are proposed for extracting texture features such as co-occurrence matrices [24], local binary patterns [25, 26], textons [27] and pattern based methods [28, 29]. These methods can be roughly classified into statistical, structural and model based method. Most of the pattern based methods attempted to retrieve the desired images based on the frequencies of each pattern in the image and treated them as feature descriptor using histograms. The frequency gives information regarding the number of times these patterns appeared in the image and it doesn't not reveal any information regarding the mutual occurrence of patterns in the image. This is addressed by the present paper by making use of textons.

The IR based on texture descriptors such as Gabor transforms [30], rotated wavelet filters [31] are proposed in the literature. The other CBIR models are based on relevance feedback techniques [32], robust local patterns [33], temporal patterns of video sequences [34] and the combination of relevance feedback with region based features [35]. Recently various pattern based features i.e. local maximum edge patterns [36], local tetra patterns [37] for natural IR are proposed. The pattern based features are also proposed for retrieving of medical images i.e. directional binary wavelet pattern [38], local mesh patterns [39] and local ternary co-occurrence patterns [40]. The block based methods using LBP texture descriptors are proposed by Takalo et al. [41] for CBIR. The present paper divides the image into multi regions and evaluates the features on each region. This provides the detailed relative location similarity and



reduces the computational complexity. The earlier works on CBIR treated the texture and color information as individual features. In this work region based rotational invariant texture features are integrated with shape and color space components for efficient image retrieval.

The present paper is organized as follows. The second section describes the concepts of basic LBP and generation of rotational invariant uniform LBP. The section three describes the methodology and frame work. The section four and five gives the results and discussions and conclusions.

2. Local binary pattern (LBP)

Ojala et al. [42] introduced a powerful local gray scale descriptor called LBP for texture classification. LBP utilizes the intensity distribution of local neighborhood pixels. The LBP code on a neighborhood is computed by comparing the greyscale value of neighboring pixels (g_p) with central pixels (g_c) as shown in the Figure 1, based on the following equations.

$$LBP_{P,R} = \sum_{p=1}^{P-1} 2^{(p-1)} * s(g_p - g_c) \quad (1)$$

$$s(x) = \begin{cases} 1 & \text{if } x \geq 0 \\ 0 & \text{otherwise} \end{cases} \quad (2)$$

Where P is the number of neighboring pixels and R is the radius of the neighborhood. A 3x3 neighborhood will have P=8 and R=1. The co-ordinates of the neighborhood pixels are computed as $(R\cos(2\pi P/P), -R\sin(2\pi P/P))$ and their grey levels are estimated by interpolation.

25	45	92	0	0	1	2 ⁰	2 ¹	2 ²	156
89	55	102	1		1	2 ⁷		2 ³	
17	29	110	0	0	1	2 ⁶	2 ⁵	2 ⁴	
(a) 3x3 neighborhood, P=8, R=1			(b) Binary pattern based on eq.2			(c) Corresponding weights			(d) LBP code generation

Figure 1: LBP code generation.

2.1 Derivation of Rotational Invariant ULBP (ULBP^{ri})

LBP with P neighboring pixels results into 2^P combinations of LBPs. This results a feature vector length of 2^P . As the number of neighboring pixels increases (16, 1) and (16, 2) the length of feature vector increases drastically. The disadvantage of this feature vector is its computational cost. To overcome this uniform LBP (ULBP) [43, 44] are proposed. The ULBPs have limited discontinues i.e. less than or equal to two in the circular binary representation and it is proved that most of the windows (above 90%) in human faces and textures are ULBPs. The remaining patterns where the numbers of transitions from 0 to 1 or 1 to 0 are above two are considered as non-ULBPs (NULBP). The NULBPs are treated as miscellaneous. There will be $P*(P-1) + 3$ distinct ULBP on a neighborhood with P neighboring pixels.

The LBP_{8,1} operator produces 2^8 different binary patterns and this results a total of 256 LBP codes or feature vector of length 256. When the image is rotated, the gray level values of P_i will correspondingly move along the perimeter of the circle around, the central pixel P_c . The pixel P_1 of the neighborhood is mostly assigned the co-ordinate position (0, 0) as shown in Figure 2. Rotating a particular binary pattern on the perimeter naturally results different LBP₈ codes. This does not apply to the constant binary pattern i.e. contains all zeros or all ones (00000000 or 11111111). To overcome this rotation effect and to make the local binary pattern as rotation invariant a unique identifier is denoted by obtaining the minimum or maximum value by rotating as given in equation 3 and 4.

$$LBP_8^{ri} = \min\{ROR(LBP_8, i) \mid i = 0, 1 \dots 7\} \quad (3)$$

or

$$LBP_8^{ri} = \max\{ROR(LBP_8, i) \mid i = 0, 1 \dots 7\} \quad (4)$$

Where ROR(z,i) performs a circular bitwise right shift on the 8-bit binary number z, i times. The min(x) or max(x) takes out the minimum or maximum LBP code from these 8- circular shifts. This becomes the rotation invariant LBP (LBP^{ri}).

(0,0)	(0,1)	(0,2)
(1,0)	(1,1)	(1,2)
(2,0)	(2,1)	(2,2)

Figure 2: The basic co-ordinate system of a LBP window.

Table 1: ULBP^{ri} values and indexes on LBP_{8,R}.

Rotational invariant ULBP on a 3 x 3 window (adjacent 1s)	LBP code Value according to equation 3	Index value assigned to ULBP ^{ri}
(0000 0001)	1	1
(00000011)	3	2
(00000111)	7	3
(00001111)	15	4
(00011111)	31	5
(00111111)	63	6
(01111111)	127	7
(11111111)	255	8
(00000000)	0	9
All others- NULBPS		0

There are 36 unique rotation invariant LBPs that occur on a 3x3 neighborhood or LBP_{8,R}. It is experimentally shown that $LBP_{8,R}^{ri36}$ does not show any good discrimination [44]. The performance of these 36 patterns in discrimination of textures varies greatly because some patterns sustain rotation quite well while other patterns do not and confuse the analysis.



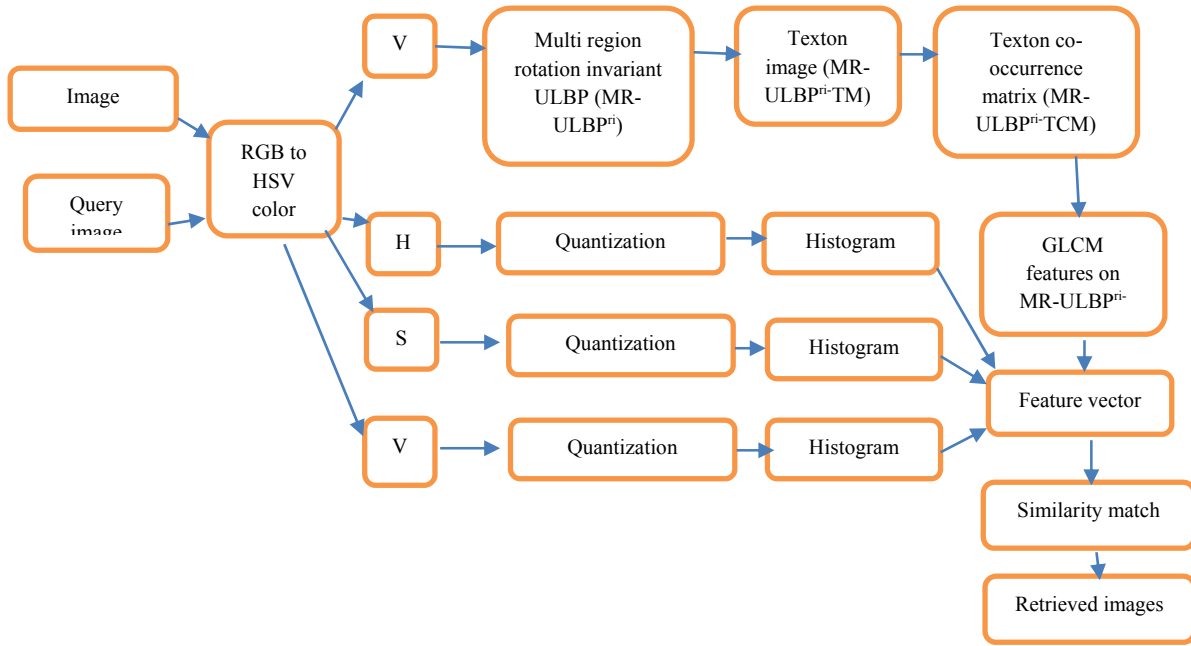


Figure 3: The integrated CBIR model of the present paper

The varying performance of these LBP^ri also led to the discovery of uniform (U) patterns. A $ULBP$ appears on a $LBP_{8,R}$, whenever there are zero or more (≤ 8) adjacent ones in any position and the Table1 summarizes the index values that are assigned to $ULBP^ri$ by the present paper.

3. Methodology

The present paper proposes a novel frame work for CBIR called “multi-region rotational invariant uniform LBP texton matrix” (MR- $ULBP^ri$ -TM) to overcome the limitations of LBP, and to capture shape information on multi regions. The basic image retrieval model of this paper is given in Figure 3.

The basic LBP operator has the following disadvantages. It is designed for a small spatial support area (3×3 neighborhood); therefore the bit-wise comparison between two single pixel values of this neighborhood is affected by noise to a great extent. The features computed on the basic LBP cannot capture larger scale structure (macrostructure) that may have dominant features of textures. In this paper the computation on sub regions is performed based on average values of sub regions, instead of individual pixels.

3.1. Computation of MR- $ULBP^ri$

The present paper converts the color image in to HSV color space and derives color histograms. The V color space of the image is divided into non over-lapped regions of size 9×9 . Each region is sub divided into nine

non overlapped sub-regions. The present multi region (MR) IR model derives a single value for each rectangular sub region. The advantage of the present method is it reduces the overall dimension space of the derived features. The MR model captures the dominant features on a large scale rectangular structure and the sub region features are estimated on grey level values of a local neighborhood. The steps for computation of MR- $ULBP^ri$ are given below.

Step one: Replace the each sub region by its average grey level value. By this the region of size 9×9 with 9 sub regions becomes a 3×3 neighborhood, where each pixel value represents the average grey level value of that sub region.

Step two: Computation of LBP on each region by average operator. The comparison operator between single pixels in LBP is simply replaced with comparison between average gray-values of sub-regions (threshold). This generates a binary pattern.

Step Three: If the generated multi region-Local binary pattern of step two is $ULBP$ then replace the central pixel with MR- $ULBP^ri$ index value as given in table 1. Otherwise replace the central pixel with value zero (NULBP).

Note that the scalar values of averages over blocks can be computed very efficiently [45] from the summed-area table [46] or integral image [47]. For this reason, MR- $ULBP^ri$ feature extraction can also be very fast: it only incurs a little more cost than the original 3×3 LBP operator. This way, MR- $ULBP^ri$ code presents several



advantages: (1) It is rotational invariant and robust; (2) it encodes not only micro structures but also macrostructures of image patterns, and hence provides a more complete image representation than the basic LBP operator; (3) MR-ULBP^{ri} can be computed very efficiently using integral images. 4) This representation is very useful in deriving textons because the image is quantized to ten levels (0 to 9); the ULBP^{ri} will be given indexes from 1 to 9 and all NULBPs as zero.

The regions can be small, medium and large i.e. 3×3 , 9×9 and 15×15 neighborhoods respectively. For a small scale regions like basic LBP, local, micro patterns of textures are well represented, which may be beneficial for discriminating local details. On the other hand, using average values over the large scale regions (15×15) reduce noise, and makes the representation more robust; and large scale information provides complementary information to small scale details and much discriminative information is also dropped. Normally, regions of various scales should be carefully selected and then fused to achieve better performance. The present paper chose a region of size 9×9 and sub regions of size 3×3 .

3.2. Computation of “Texton Matrix on Multi Region Rotational Invariant Uniform LBP (MR-ULBP^{ri}-TM)”

The previous section generates a multi-region based ULBP^{ri} (MR-ULBP^{ri}) image with ten quantized levels or patterns {0 to 9}. The present section evaluates textons on this. The LBP and texton based models are widely used in many applications [48, 49, 50, 51]. It is found that, it is very difficult to obtain satisfactory results, of image processing, by designing algorithms that process the images based on pixel levels. More over this processing system fail in representing the shape component totally. To address this Julesz [27] proposed the concept of texton's. Textons represent the relationship between pixels in the form of shape component; however defining a texton is still a difficult task. Texton is one of the popular and significant shape primitives and is defined with certain placement rule. The textons represents the emergent and dominant patterns on a local neighborhood.

The image features have a close relationship with textons and color diversification. The difference textons may form various image features. If the textons in image are small and the tonal differences between neighboring textons are large, a fine texture may result. If the textons are higher and holds quite a few pixels then it results a coarse texture and it also depends on scale [49]. In the image if the textons are large and contains a small number of texton categories, then a shape may result. There can be numerous types of textons in image. In this paper, we only classify and make use of five special types of textons that holds all the three or four

neighboring pixels on a 2×2 windows or grid. The pixels of the grid are denoted as P, Q, R and S. The five types of textons are denoted as A_1 , A_2 , A_3 , A_4 and A_5 (Figure 4).

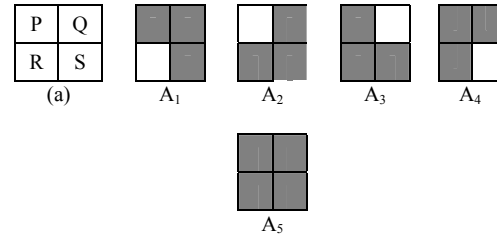
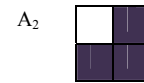
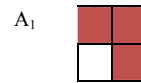


Figure 4: The textons used in this paper (a) 2×2 window of the image A_1 to A_5 : different textons.

0	1	2	4	4	8	9
2	1	1	8	5	9	9
4	4	7	5	5	8	8
4	4	2	2	1	0	8
5	0	4	2	8	0	3
5	5	7	7	5	6	6
2	1	7	9	9	6	8

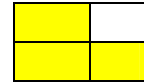
(a)



0	0	0	0	0	0	0
0	0	0	0	0	0	0
4	4	0	0	8	8	8
0	4	0	0	0	0	8
0	0	0	0	0	0	0
0	0	7	7	0	0	0
0	0	7	0	0	0	0

0	0	0	0	0	0	9
0	0	0	0	5	9	9
0	4	0	5	5	0	0
4	4	0	0	0	0	0
0	0	0	0	0	0	0
0	0	0	0	0	0	0
0	0	0	0	0	0	0

A_3



0	1	0	0	0	0	0
0	1	1	0	0	0	0
4	0	0	0	0	0	0
4	4	0	0	0	0	0
5	0	0	0	0	0	0
5	5	0	0	0	0	0
0	0	0	0	0	0	0

(b)



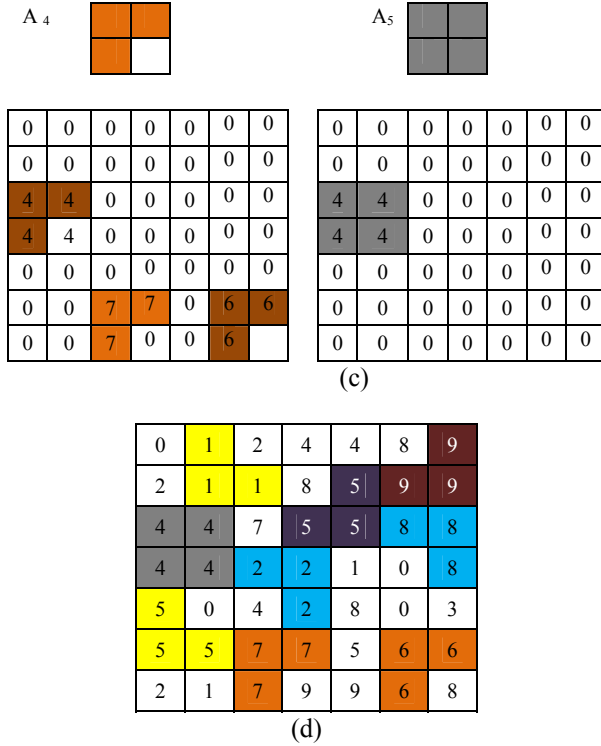


Figure 5: computation of MR-ULBP^{ri}-TM from MR-ULBP^{ri} image. (a):MR-ULBP^{ri} image ; (b):Detection of textons A₁, A₂ and A₃ on MR-ULBP^{ri} image (c)Computation of textons A₄ and A₅ on MR-ULBP^{ri} image; (d)Formation of MR-ULBP^{ri}-TM (Final Texton image) using A₁, A₂, A₃, A₄ and A₅.

The process of texton identification is shown in Figure 5. The present paper used the five types of textons to detect every grid. A particular texton detection process is performed on a 2 x 2 grid in overlapped manner (shifting right by one column position then row by one position down) and if the texton is detected the pixels of texton are kept with original values and others are replaced with zeros. The same process is repeated for all five defined categories of textons. The MR-ULBP^{ri}-TM (final texton) image (Figure 5(d)) will be formed by combining these five types of texton images (Figure 5(b) & 5(c)).

3.3 COMPUTATION OF GLCM FEATURES ON MR-ULBP^{ri}-TM

On MR-ULBP^{ri}-TM image, the co-occurrence matrix is formed with a distance D and with an angle 0°, 45°, 90° and 135°. The GLCM features i.e. entropy, energy, contrast, local homogeneity and correlation (equations 5, 6, 7, 8 and 9) are computed on MR-ULBP^{ri}-TM with 0°, 45°, 90° and 135° orientations and average feature values of these orientation are listed in the feature library. In order to extract color information the present paper also quantized the original image using HSV color space.

$$\text{Entropy} = \sum_{i,j=0}^{N-1} -\ln(P_{ij})P_{ij} \quad (5)$$

$$\text{Energy} = \sum_{i,j=0}^{N-1} -\ln(P_{ij})^2 \quad (6)$$

$$\text{Contrast} = \sum_{i,j=0}^{N-1} P_{ij} (i - j)^2 \quad (7)$$

$$\text{Local Homogeneity} = \sum_{i,j=0}^{N-1} \frac{P_{ij}}{1 + (i-j)^2} \quad (8)$$

$$\text{Correlation} = \sum_{i,j=0}^{N-1} P_{ij} \frac{(i-\mu)(j-\mu)}{\sigma^2} \quad (9)$$

where P_{ij} is the pixel value in position (i,j) of the texture image, N is the number of gray levels in the image, μ is $\mu = \sum_{i,j=0}^{N-1} i P_{ij}$ mean of the texture image and σ^2 is $\sigma^2 = \sum_{i,j=0}^{N-1} P_{ij} (i - \mu)^2$ variance of the texture image.

3.4 Image Retrieval Algorithm

The proposed image retrieval algorithm is given below

Input: Query image Output: Retrieval of similar images

1. Convert the RGB image into HSV color space.
2. Divide the v-color space image into non overlapped regions of size 9 x 9.
3. Divide the region into sub regions and derive feature vector (The region of size 9 x 9 becomes 3 x 3).
4. Derive multi region rotational invariant ULBP (MR-ULBP^{ri}) index (as given in table 1) image.
5. Compute texton matrix on multi-region rotational invariant ULBP (MR-ULBP^{ri}-TM) by deriving textons on each 2x2 grid of step 4.
6. Derive multi-region rotational invariant ULBP texton co-occurrence matrix (MR-ULBP^{ri}-TCM) with various distances on step 5.
7. Compute GLCM features on MR-ULBP^{ri}-TCM.
8. Compute the histograms for H, S and V color spaces.
9. Construct feature vector by concatenating histograms for H, S and V color spaces with MR-ULBP^{ri}-TCM features.
10. Compare the features of query image with the images in the database using similarity measurement.
11. Retrieve the images based on nearest distance or best matches.

3.5 Query Matching

This is accomplished by measuring the distance between the query image and database images. The present paper used Euclidean distance as the distance measure and as given below

$$\text{Dist}_s(T_n, I_n) = \left(\sum_{i,j=1}^n |f_i(T_n) - f_j(I_n)|^2 \right)^{1/2} \quad (10)$$

Where T_n query image, I_n image in database;

The database image is used as the query image in our experiments. If the retrieved image belongs to the same category as that of query image we say that the system has suitably identified the predictable image otherwise the system fail to find the image.



4. Results and Discussion

In order to efficiently investigate the performance of the present retrieval model, we have considered the Wang database [52]. Wang is a subset of Corel stock photo database. In the Wang database the images have been manually chosen. This data base consists of 5 classes of images i.e. Elephants, Fancy Flowers, Horses, Valleys and Evening Skies and 100 images per each class. The present paper used these 5 classes of images for relevance assessment. For a query image the relevant images are assumed to be the remaining 99 images of the same class. The images from all other classes are treated as irrelevant images. The hefty size of each class and the heterogeneous image class contents made Wang data base as one of the popular database for image retrieval. The performance of the present model is evaluated in terms of precision and recall rate. Precision is the ratio of number of retrieved images (I_{NR}), Vs. the number of relevant images retrieved (I_{RR}). The recall is the ratio of total number of relevant images in the database (I_{TR}) Vs. I_{RR} .

$$\text{Precision} - P = (I_{RR} / I_{NR}) \quad (11)$$

$$\text{Recall} - R = (I_{RR} / I_{TR}) \quad (12)$$

The present paper compute GLCM features on MR-ULBP^{ri}-TCM using various distance values: $D = 1, 2, \dots, 7$ and query matching is performed using Euclidean distance. The present retrieval model selects 16 top images from the database images that are matching with query image. And also experimented with more number of top images and retrieval performance is measured. Figure 6 shows five examples of retrieval images, i.e. one image from each class, by the proposed method with $D=4$ for $I_{NR}=16$ and top left most image is the query image.

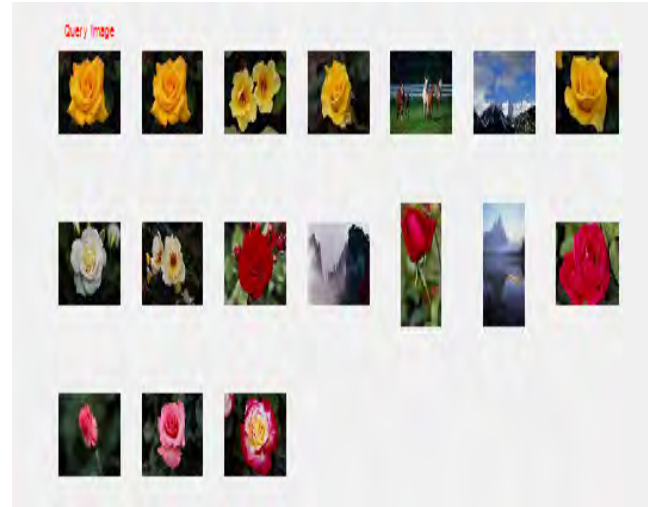


Figure 6 (b): Retrieved fancy flower images.

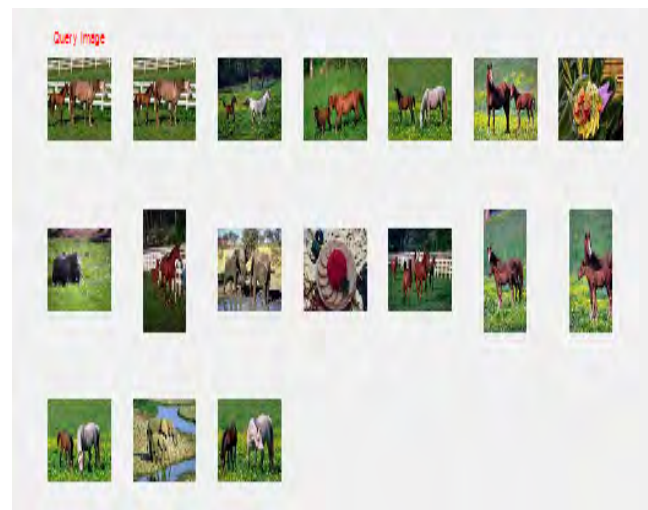


Figure 6(c): Retrieved horse images.

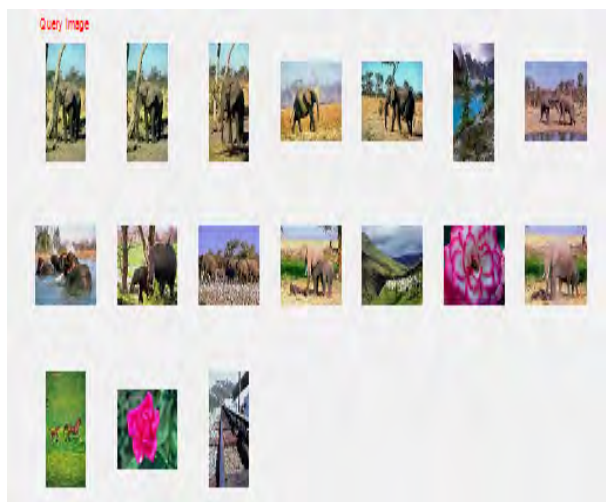


Figure 6 (a): Retrieved elephant images.

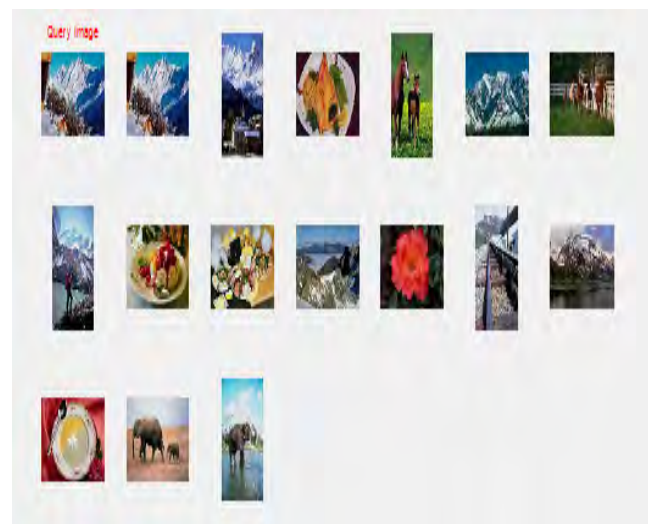


Figure 6 (d): Retrieved valley images.



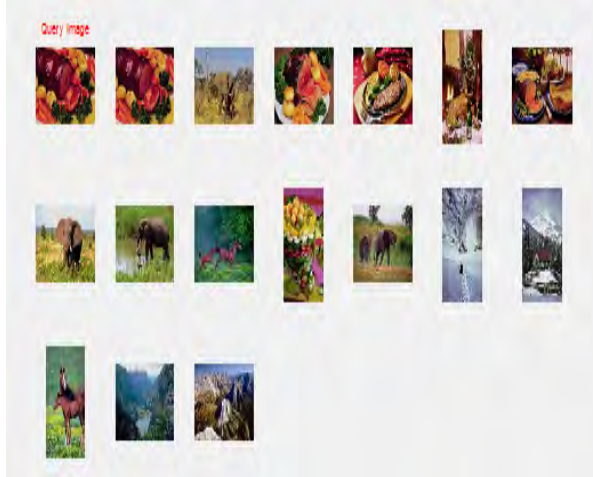


Figure 6 (e): Retrieved Evening Skies images.

Fig 6(a) to 6(e) Retrieved images for each class with $D=4$ for $I_{NR}=16$ on proposed integrated method.

The average precision and recall rates of all classes of images are computed based on MR-ULBP^{ri}-TCM features and color histograms and listed in Tables 2 and 3. The best performance of MR-ULBP^{ri}-TCM with color histograms was obtained when $D=4$. The retrieval performance of the integrated MR-ULBP^{ri}-TCM is compared with GLCM [53], color correlogram [54] and texton Co-occurrence matrix [49]. The present paper selected 60 images of the same category or class as query images (one by one) and computed precession and recall rates by selecting top 16, 25, 35, 45, 55, 65, 75, 85 and 95 images. The average precession rates of GLCM, CCG and TCM are ranging from 38% to 45%, 39% to 46% and 60% to 64% respectively for $D=4$ and for number of images retrieved $I_{NR}=16$ (Table 2 & 3). The average precession and recall rates are plotted in graphs (Figure 7 and 8) by varying I_{NR} . The present paper also computed image retrieval accuracy as defined below.

$$IR \text{ accuracy } A = ((\text{precession} + \text{recall}) / 2) \quad (11)$$

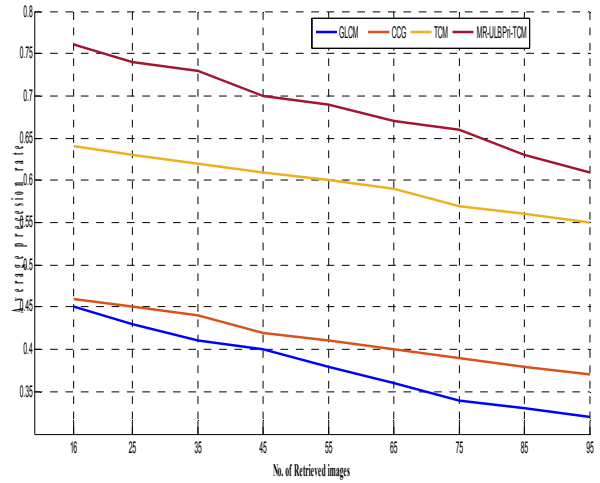
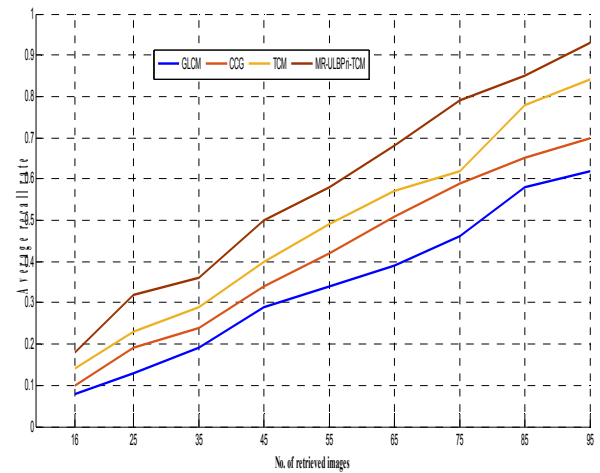
Table 2: Average precision rate of all classes of images with various distance measures for $I_{NR}=16$.

Methods	Distance parameter						
	D=1	D=2	D=3	D=4	D=5	D=6	D=7
GLCM	0.38	0.41	0.42	0.45	0.44	0.43	0.43
CCG	0.39	0.41	0.44	0.46	0.45	0.44	0.43
TCM	0.60	0.61	0.63	0.64	0.63	0.61	0.62
Proposed MR-ULBP ^{ri} -TCM	0.69	0.71	0.74	0.76	0.75	0.72	0.71

The average IR accuracy graph with varying number of matches considered (I_{NR}) is plotted (Figure 9). The proposed integrated MR-ULBP^{ri}-TCM achieved best performance when compared to the existing three methods.

Table 3: Average precession rate on each class of images for $D=4$ for $I_{NR}=16$.

Methods	Image category and the precision (%)					
	Elephants	Fancy Flowers	Horses	Valleys	Evening Skies	Average
GLCM	0.39	0.42	0.44	0.48	0.5	0.45
CCG	0.4	0.43	0.46	0.49	0.52	0.46
TCM	0.61	0.6	0.66	0.67	0.7	0.64
Proposed MR-ULBP ^{ri} -TCM	0.71	0.72	0.76	0.81	0.82	0.76

Figure 7: Average Performance curve (precision) using GLCM, CCG, TCM and MR-ULBP^{ri}-TCM method with $D=4$.Figure 8: Average Performance curve (recall) using GLCM, CCG, TCM and MR-ULBP^{ri}-TCM method with $D=4$.

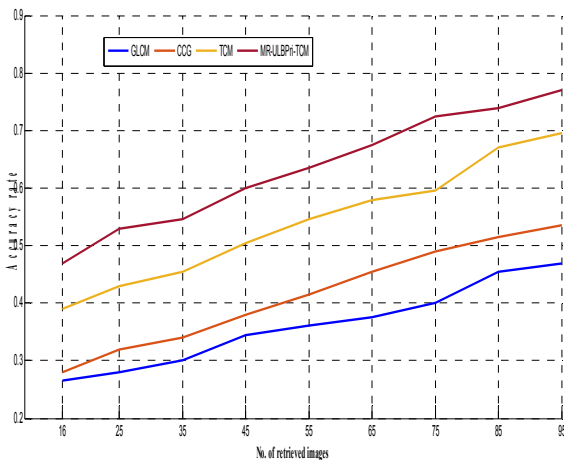


Figure 9: Average Performance curve (accuracy) using GLCM, CCM, TCM and MR-ULBP-TCM method with $D=4$.

5. Conclusions

The proposed CBIR model integrated the features from texture, shape and color. The present paper derived a region based model and evaluated rotational invariant features in the form of ULBP^{ri}. The proposed model is robust and averages can be computed efficiently using integral images. The small feature set of multi region can make the overall process to be simple and suitable when dealing with large size images especially in real time environment. The rotational invariant ULBP indexing quantizes the image in to 10 levels and these are useful in computing texton matrix. The GLCM features derived on MR-ULBP^{ri}-TCM along with color histograms outperformed the earlier methods of image retrieval. The proposed method is carried out with varying distances and number of retrieved images. The proposed method shown high results of retrieval for $D=4$.

REFERENCES

- [1] H.B. Kekre, S.D. Thepade, "Color traits transfer to grayscale images", in: IEEE Int. Conference on Emerging Trends in Engineering and Technology, ICETET, 2008.
- [2] C.M. Pun, C.F. Wong, "Fast and robust, color feature extraction for content-based image retrieval", Int. J. Adv. Comput. Technol. 3 (6) (2011).
- [3] L. Cinque, G. Ciocca, S. Levialdi, A. Pellicano, R. Schettini, "Colour-based image retrieval using spatial-chromatic histogram", Image Vis. Comput. 19 (2001), pp: 979–986.
- [4] R. Krishnamoorthi, S. Sathiyadevi, "A multi resolution approach for rotation invariant texture image retrieval with orthogonal polynomials model", J. Visual Commun. Image Represent. 23 (1) (2012), pp: 18–30.
- [5] G. AlGarni, M. Hamiane, "A novel technique for automatic shoeprint image retrieval", Forensic Sci. Intern. 181 (2008), pp:10–14.
- [6] S. Jeong, C.S. Won, R.M. Gray, "Image retrieval using color histograms generated by Gauss mixture vector quantization", Computer Vision Image Understanding, Vol-94, iss-1-3, june-2004, pp:44-66.
- [7] J. Yue, Z. Li, L. Liu, Z. Fu, "Content-based image retrieval using color and texture fused features", Math. Comput. Modelling 54 (2011), pp: 1121–1127.
- [8] C.H. Lin, R.T. Chen, Y.K. Chan, "A smart content-based image retrieval system based on color and texture feature", Image Vis. Comput. 27 (6) (2009) pp: 658–665.
- [9] V. Vijaya Kumar, U.S.N. Raju, K. Chandra Sekharan, V.V. Krishna, A new method of texture classification using various wavelet transforms based on primitive patterns, ICGST-Graphics, vision and image processing (ICGST-GVIP), Vol.8, No. 2, pp.21-27, July-2008
- [10] V.Vijaya Kumar, B. Eswar Reddy, U.S.N. Raju, A.Suresh, Classification of textures by avoiding complex patterns, Journal of computer science, Science publications, Vol.4, No.2, pp.133-138, Feb-2008
- [11] V Vijaya Kumar, U S N Raju, K Chandra Sekaran, V V Krishna, Employing long linear patterns for texture classification relying on wavelets, ICGST-Graphics, vision and image processing (ICGST-GVIP), Vol.8, No.5, pp. 13-21, Jan-2009.
- [12] P.Viala, M.J. Jones, Robust real time face detection, Int. J. Comput. Vis.57 (2), (2004), 2063-2077.
- [13] K. Srinivasa Reddy, V.Vijaya Kumar, B.Eshwara reddy, Face Recognition based on Texture Features using Local Ternary Patterns", I.J. Image, Graphics and Signal Processing, 2015, 10, 37-46, ISSN: 2074-9082.
- [14] Feiniu Yuan, A double mapping framework for extraction of shape-invariant features based on multi-scale partitions with AdaBoost for video smoke detection, Pattern Recgni. 45(12), (2012), 132-139
- [15] V. Vijaya Kumar P. Chandra Sekhar Reddy B. Eswara Reddy, New method for classification of age groups based on texture shape features, International journal imaging and robotics, Vol. 15, No.1, 2015,
- [16] G S Murty, J Sasi Kiran, V.Vijaya Kumar, Facial expression recognition based on features derived from the distinct LBP and



- GLCM, International journal of image, graphics and signal processing (IJIGSP), , Vol.2, No.1, pp. 68-77,2014, ISSN: 2074-9082.
- [17] Yanwu Xu, Xianbin Cao, Hong Qiao, An efficient tree classifier ensemble-based approach for pedestrian detection, IEEE Trans. Syst. Man Cybern., Part B, Cybern, 41 (1) (2011) 107-117
- [18] Markus Enzweiler, Dariu M.Gavrila, A multilevel mixture-of-experts frame work for pedestrian classification, IEEE Trans. Image. Proc. 20 (10) (2011), 2967-2979
- [19] Roland Kwitt, Peter Meerwaid, Andreas, Uhl, Efficient texture image retrieval using copulas in a Bayesian frame work, IEEE Trans. Image Process, 20 (7), (2011) 2063-2077
- [20] A Obulesu,JS Kiran, VV Kumar, Facial image retrieval based on local and regional features, IEEE- 2015 International Conference on Applied and Theoretical Computing and Communication Technology (iCATccT), 29-31 Oct. 2015, Pp:841 - 846
- [21] Nidhi Goel and Ekta Walia, Fast Content Based Image Retrieval Using Zernike Moments, Graphics, Vision and Image Processing Journal, ISSN 1687-398X, Volume 16, Issue 1, ICGST LLC, Delaware, USA, June 2016
- [22] Said Jai-Andaloussi, Mathieu Lamard, Guy Cazuguel, Hamid Tairi, Mohamed Meknassi, Christian Roux, Béatrice Cochener, Content Based Medical Image Retrieval Based on BEMD: use of Generalized Gaussian Density to model BIMFs coefficients, ICGST-GVIP Journal, Volume 10, Issue 2, June 2010
- [23] S. Djerroud and L. Zaoui, Segmentation of Heterogeneous Image Database for Amelioration of Content Based Image Retrieval by Data Mining Method, GVIP-ICGST Journal, Volume 9, Issue 6, December 2009
- [24] Chinmei Qing, Jianmin Jiang, Zhuhubg Yang, Normalized co-occurrence mutual information for facial pose detection inside videos, IEEE Trans., Circuits Syst. Video Technol. 20 (12) (2010) 1898-1902
- [25] Feiniu Yuan, Video-based smoke detection with histogram sequence of LBP and LBPV pyramids, Fire Saf. J. 46., (3) (2011) 132-139
- [26] T. Ojala, M.Pietikainen, T.T. Maenapaa, Multiresolution gray-scale and toation inavreint texture classification with local binary pattern, IEE Trans. Pattern Anal. Mach. Intell. 24(7), (2002), 971-987
- [27] B. Julesz, "Textons, the elements of texture perception, and their interactions", Nature 290 (5802) (1981) 91-97.
- [28] V. Vijaya Kumar Jangala. Sasi Kiran G.S.Murthy, Pattern based dimensionality reduction model for age classification, International journal of computer applications (IJCA), Vol.79, No.13, pp. 14-20, Oct-2013, ISSN: 0975-8887.
- [29] Vishnu Murthy. G, V. Vijaya Kumar, B.V. Ramana Reddy, Employing simple connected pattern array grammar for generation and recognition of connected patterns on an image neighborhood, ICGST-Graphics vision and image processing, (ICGST-GVIP) Vol.14, No.1, pp. 39-44, Aug-2014
- [30] B.S. Manjunath, W.Y. Ma, Texture features for browsing and retrieval of image data, IEEE Trans. Pattern Anal. Mach. Intell. 18 (8) (1996) 837-842.
- [31] M. Kokare, P.K. Biswas, B.N. Chatterji, Texture image retrieval using rotated wavelet filters, Pattern Recogn. Lett. 28 (2007) 1240-1249.
- [32] N. Hossein, K. Ehsanollah, Concept learning by fuzzy k-NN classification and relevance feedback for efficient image retrieval, Expert Syst. Appl. 36 (2009) 5948-5954.
- [33] Subrahmanyam Murala, Q.M. Jonathan Wu, Expert content-based image retrieval system using robust local patterns, J. Vis. Commun. Image R. 25 (2014) 1324-1334
- [34] Ja-H. Su, Yu-T. Huang, Hsin-H. Yeh, S.T. Vincent, Effective content-based video retrieval using pattern-indexing and matching techniques, Expert Syst. Appl. 37 (2010) 5068-5085.
- [35] Wan-Ting Su, Ju-Chin Chen, Jenn-Jier James Lien, Region-based image retrieval system with heuristic pre-clustering relevance feedback, Expert Syst. Appl. 37 (2010) 4984-4998.
- [36] M. Subrahmanyam, R.P.Maheshwari, R. Balasubramanian, Local maximum edge binary patterns: a new descriptor for image retrieval and object tracking, Signal Process. 92 (2012) 1467-1479.
- [37] M. Subrahmanyam, R.P. Maheshwari, R. Balasubramanian, Local tetra patterns: a new feature descriptor for content based image retrieval, IEEE Trans. Image Process. 21 (5) (2012) 2874-2886.
- [38] M. Subrahmanyam, R.P. Maheshwari, R. Balasubramanian, Directional binary wavelet patterns for biomedical image indexing and



- retrieval, *J. Med. Syst.* 36 (5) (2012) 2865–2879.
- [39] M. Subrahmanyam, Q.M. JonathanWu, Local mesh patterns versus local binary patterns: biomedical image indexing and retrieval, *IEEE J. Biomed. Health Inform.* 8 (3) (2014) 929–938.
- [40] M. Subrahmanyam, Q.M. Jonathan Wu, Local ternary co-occurrence patterns: a new feature descriptor for MRI and CT image retrieval, *Neurocomputing* 119 (7) (2013) 399–412.
- [41] V. Takala, T. Ahonen, M. Pietikainen, Block-based methods for image retrieval using local binary patterns, *LNCS* 3450 (2005) 882–891.
- [42] T.Ojala, M. Pietikäinen, and D. Harwood, “A comparative study of texture measures with classification based on featured distributions,” *Pattern Recognition*, vol. 29, no. 1, 1996, pp. 51-59
- [43] Z.Guo, L.Zhang,D.Zhang, Rotation invariant texture classification using LBP variance with global matching, *Pattern Recognition*, 43, (2010), 706-716
- [44] Pietikäinen, M., Ojala, T., Xu. Z.: Rotation-Invariant Texture Classification Using Feature Distributions. *Pattern Recognition* 33 (2000) 43-52
- [45] Simard, P.Y., Bottou, L., Haffner, P., Cun, Y.L.: Boxlets: a fast convolution algorithm for signal processing and neural networks. In: Kearns, M., Solla, S., Cohn, D. (eds.) *Advances in Neural Information Processing Systems*, vol. 11, pp. 571–577. MIT Press, Cambridge (1998)
- [46] Crow, F.: Summed-area tables for texture mapping. In: *SIGGRAPH*, vol. 18(3), pp. 207–212 (1984)
- [47] Viola, P., Jones, M.: Robust real time object detection. In: *IEEE ICCV Workshop on Statistical and Computational Theories of Vision*, Vancouver, Canada, July 13, 2001 (2001)
- [48] U Ravi Babu,V Vijay Kumar,BSujatha,Texture classification based on texton features *International journal of image, graphics and signal processing (IJIGSP)*, Vol.4, No.8, pp.36-42, Auguest-2012, ISSN: 2074-9074.
- [49] Guang-Hai Liu, Jing-Yu Yang, Image retrieval based on the texton co-occurrence matrix, *Pattern Recognition*, 41(12) (2008)3521-3527.
- [50] Guang-Hai Liu , Lei Zhang, Ying-Kun Hou, Zuo-Yong Li, Jing-Yu Yang, Image retrieval based on multi-texton histogram, *Pattern Recognition* 43 (2010) 2380–2389
- [51] B.Eswara Reddy, P.Chandra Sekhar Reddy, V.Vijaya Kumar, Texton based shape features on local binary pattern for age classification, *International journal of image, graphics and signal processing (IJIGSP)*, Vol. 7, No.4,pp.54-60, July-2012
- [52] Corel 1000 image database. [Online]. <<http://wang.ist.psu.edu/docs/related.shtml>>
- [53] R.M. Haralick, K. Shangmugam, I. Dinstein, Textural feature for image classification, *IEEE Trans. Syst. Man Cybern. SMC-3* (6) (1973) 610–621.
- [54] J. Huang, S.R. Kumar, M. Mitra, et al., Image indexing using color correlograms, in: *IEEE Conference on Computer Vision and Pattern Recognition*, 1997, pp. 762–768.



Biographies



Talluri. Sunil Kumar received his M.Tech Degree in Computer Science & Engineering from Osmania University Hyderabad, Telangana State, India. He is an Associate Professor in Computer Science & Engineering Department, VNR Vignana Jyothi Institute of Engineering and Technology, Hyderabad, Telangana State, India. He Published 2 publications in various National and International Journals/Conferences. Organised International Conferences. His main research interest includes, Data Mining Image Processing, Cloud Computing, Machine Learning. He is a life member of CSI, ISTE.



Dr. T.V.Rajinikanth received M.Tech Degree in Computer Science & Engineering from Osmania University Hyderabad, Telangana, India and he received PhD degree from Osmania University Hyderabad, Telangana, India. He is Professor of Computer Science & Engineering Department, SNIST, Hyderabad, Telangana, India. Published more than 50 publications in various National and International Journals/Conferences. Organised and Program Chaired 2 International Conferences, 2 grants received from UGC, AICTE. Editorial Board Member for several International Journals. Received Best Paper Award : “Design and Analysis of Novel Similarity Measure for Clustering and Classification Of High Dimensional Text Documents” in the Proceedings of 15th ACM-International Conference on Computer Systems and Technologies (CompSysTech-2014), pg:1-8, 2014, Ruse, Bulgaria, Europe. His main research interest includes Image Processing, Data Mining, Machine Learning.



Dr. B. Eswara Reddy Graduated in B.Tech.(CSE) from Sri Krishna Devaraya University in 1995. He received Masters Degree in M.Tech.(Software Engineering), from JNT University, Hyderabad, in 1999. He received Ph. D in Computer Science & Engineering from JNT University, Hyderabad, in 2008. Currently, he is working as Professor in CSE Department & Principal of JNTU-A College of Engineering, Kalikiri, Chittoor Dist A.P, India. He has published more than 100 publications in National and International Conferences and Journals. His research interests include Pattern Recognition & Image Analysis, Data Mining, and Cloud Computing. He received UGC Major Research Project titled ‘Cloud Computing Framework for Rural Health Care in Indian Scenario’. He is Co-author of the text books ‘Programming with Java’ (Pearson/Sanguine) and ‘Data Mining’ (Elsevier India). He is a life member of CSI, ISTE, ISCA, Fellow-IE (India) and member of IEEE







Spectral-Spatial Classification of Hyperspectral Image based on Oversampling and Multi-Feature Kernels

Rafika Ben Salem¹, Karim Saheb Ettabaa^{2,3} and Mohamed Ali Hamdi¹

¹Laboratory for Materials, Molecular and applications, National Institute of Applied Sciences and Technology, Tunis, Tunisia.

bs_rafika@yahoo.fr, mohamedalihamdi@yahoo.fr

²Laboratory for research in computer Arabized and integrated documentation, National School of Computer Sciences, Tunis, Tunisia.

³Laboratory ITI, Telecom Bretagne, Brest Iroise Technopole CS 81828
karim.sahebettabaa@riad.rnu.tn

Abstract

Spectral-Spatial classification of hyperspectral image suffers from two problems: the existence of various feature extraction methods that complicate the choice of those applying and the availability of limited number of labeled training samples. To overcome these difficulties, this paper presents new spectral-spatial classification approach for remotely sensed hyperspectral image which integrates different spectral and spatial features via multi-feature kernels and process accurately with limited number of training samples. In fact, the proposed method introduces different methods to extract the spectral and the spatial features and exploits the oversampling based on interpolation techniques to generate new labeled samples. First, each pixel must be characterized by two spectral vectors computed according to the application of the principal components analysis, the independent components analysis and three spatial features calculated by using three methods: the average of neighbourhood pixels, the textural features and the extended multi-attribute profiles. Then an oversampling step is introduced to create new labeled samples used to train the classifier. Finally, a support vector machine (SVM) with multi-feature kernel is efficiently trained to generate the classification map. The proposed classification approach is experimentally evaluated using the AVIRIS Indian Pines data set, exhibiting higher performance when compared with the multi-feature classification without oversampling.

Keywords: Hyperspectral images, SVM, multi-feature kernels, interpolation techniques.

Nomenclature:

AA	Average Accuracy
AP	Attribute Profile
ASM	Angular Second Moment
EAP	Extended Attribute Profile

ENT	Entropy
EMAP	Extended Multi-Attribute Profile
GLCM	Gray Level Co-Occurrence Matrix
ICA	Independent Components Analyses
k	Kappa coefficient
LM	Local Mean
MLR	Multinomial Logistic Regression
MP	Morphological Profiles
OA	Overall Accuracy
PCA	Principal Components Analysis
SVM	Support Vector Machine
Var	Variance

1. Introduction

Recent advances on remote sensing provide images with high spectral and spatial resolution. Hyperspectral image presents the captured scene in hundreds of narrow contiguous bands spanning the visible-to-infrared spectrum. For that, hyperspectral data are used in a diverse applications such as agriculture [1], astronomy [2], surveillance [3] and environmental sciences [4]. These applications are based on the classification of each pixel in hyperspectral imagery. The objective of the classification is to assign each pixel to one of the classes, based on its spectral and spatial characteristics. Then, the exploitation of the highly informative spectral and spatial information of hyperspectral image pixels improves the accuracy of the classification. Nevertheless, the complexity and the high dimensionality of hyperspectral data complicate the classification, thus this technique is a challenging task.

In the last decades, many discriminative classification approaches have been developed. Among these, the SVM [5] and MLR [6]–[4] have demonstrated to be very powerful. In particular, SVM has shown good performances for classifying high-dimensional data [7]. For that various spectral-spatial classification methods based on SVM have been presented in literature.



Composite kernels [8], which combine spectral and spatial kernels have been used to assure an accurate classification. The uses of stacked vector that concatenate spectral and contextual information extracted by MP has shown a significant improvements [9]. Edge-preserving filters have been exploited to develop an accurate spectral-spatial classification outperforming the classification without filtering [10]. A multi-feature model aiming at constructing a SVM set combining multiple spectral and spatial features [11] has registered an accurate classification. A generalized composite kernels have been introduced to improve the performance of the classification [12]. Segmentation techniques have been investigated in [13]. A multi-feature kernels [14], which combine different type of kernels: kernel for each feature, have noted a relevant classification.

The literature review showed that all the studies emphasized the importance of the spatial information in the hyperspectral image classification. However, the availability of various spectral and spatial characterization methods (e.g. PCA [15], ICA [16], morphological features [17], wavelet-based texture [18], GLCM [19]) complicate the selection of the used methods.

Another difficulty has been discussed in the literature, the Hughes phenomenon referred to the high dimensionality of the hyperspectral data and the availability of a limited number of training samples. Then different solutions have been proposed to solve this problem. Among these we note: the application of features selection [20] and extraction methods to reduce the dimensionality of data and the uses of semi-supervised learning techniques to develop a semi-supervised classification approach based on the augmentation of the number of training samples from the set of unlabeled pixels. Synthetic data has been investigated in [21] to increase the set of labeled samples by oversampling, which generate new samples by means of interpolation techniques.

In this context, we propose a multi-feature spectral-spatial classification approach based on oversampling aims to solve the problem of the limited number of training samples and to overcome the difficulty of the choice of the adopted characterization methods. The proposed approach implements the following three main steps: 1) spectral and spatial characterization step that introduces different methods to extract the spectral and the spatial features, 2) oversampling which exploits interpolation techniques to create new labeled examples and 3) classification step based on the use of SVM with multi-feature kernels that combine different type of kernels: kernel for each feature.

The remainder of this paper is organized as follows. Section 2 describes the proposed approach. Section 3 reports classification results based on real hyperspectral data sets. Finally, Section 4 concludes with some remarks.

2. Proposed approach

The goal of the proposed approach is to have an accurate SVM classification dealing with these two problems:

- the existence of many features extraction methods and the difficulty of the choice of the suitable method,
- the limited number of training samples.

For that, we propose to apply an oversampling step presented in [21] to increase the number of labeled pixels and to use the multi-feature kernels to combine different attributes resulted from the application of various spectral and spatial feature extraction techniques.

The proposed approach implements the following three main steps: 1) spectral and spatial characterization step that introduces different methods to extract the spectral and the spatial features, 2) oversampling step that exploits interpolation techniques to create new labeled examples and 3) classification step based on the use of SVM with multi-feature kernels.

2.1. Spectral and spatial characterization

The wealthy spectral and spatial information available in hyperspectral images allows for the possibility to distinguish between spectrally similar materials. Various methods have been widely used in the literature for spectral and spatial characterizing hyperspectral pixels. For the spectral characterization, authors usually used all the spectral information or dimensionality reduction techniques like PCA and ICA to extract the most informative data. For the spatial features extraction, different means have been adopted such as: features provided from the neighborhood of the pixel, attribute filters and textural features.

In this paper, we focus on the uses of PCA and ICA for the spectral characterization and the mean of neighborhood pixels, EMAP based on attribute filters and textural features for the spatial characterization.

- PCA: is a statistical procedure that uses an orthogonal transformation to convert a set of observations of possibly correlated variables into a set of values of linearly uncorrelated variables called principal components. Then, PCA aims to remove the correlation among the bands. In the process, the optimum linear combination of the original bands accounting for the variation of pixel values in an image is identified.
- ICA: is a popular approach to blind source separation, it has been investigated in the analyse of hyperspectral images to remove the dependence between bands.
- Average of neighbourhood pixels: this spatial characterization technique explains each pixel (p) in terms of its neighborhood (p_k) in a window ($i*j$) by calculating the average of their spectral information $X(p_k)$. It return X_{avg} (Equation (1)).

$$X_{avg}(p) = \frac{1}{i*j} \sum_{k=1}^{i*j} X(p_k) \quad (1)$$

- Textural features [22]: emphasize the texture structure of the graylevel image. They are local indexes computed by means of sliding windows of size $P \times Q$. For hyperspectral image, these metrics can be found by adopting the panchromatic band, the first principal component or a discriminative band. Among these features we can note:

- Local mean (LM): is computed on the graylevel values contained in the sliding window centered on the pixel x_{ij} . It return a local texture value x_{ij}^{LM} (Equation (2)).



$$x_{ij}^{LM} = \frac{1}{PQ} \sum_{p,q \in w} x_{pq} \quad (2)$$

where w denotes the pixels contained in the window centered on x_{ij} .

- Variance (Var): It return a local texture value x_{ij}^{Var} (Equation (3))

$$x_{ij}^{Var} = \frac{1}{PQ} \sum_{p,q \in w} (x_{pq} - x_{ij}^{LM})^2 \quad (3)$$

where w denotes the pixels contained in the window centered on x_{ij} and x_{ij}^{LM} the local mean of the considered pixel.

- Entropy (ENT): This measure compute the intensity of the texture in the considered image. It is based on the GLCM, that represents the relative occurrence frequency $p(m, n)$ of two graylevel intensities m and n in the $P \times Q$ window at a given angular neighbourhood (Equation (4)).

$$x_{ij}^{ENT} = - \sum_{n_1} \sum_{n_2} p(n_1, n_2) \log p(n_1, n_2) \quad (4)$$

-Angular second moment (ASM): It indicates the local contrast, providing an accurate estimate on the degree of uniformity of the values of the GLCM (Equation (5)).

$$x_{ij}^{ASM} = \sum_{n_1} \sum_{n_2} p(n_1, n_2)^2 \quad (5)$$

- EMAP [23] is a profile that stacked the EAPs obtained using different type of attributes. The EAP is resulted by generating an AP (obtained by applying a sequence of attribute filters using various thresholds) on each of the first p principal components.

2.2. Oversampling

To increase the number of training samples, we implemented the oversampling algorithm (Algorithm 1) [21]. The goal of this algorithm is to generate from the t feature vectors y_i of dimension dim presenting the set of training samples ($Y^{train} = (y_1, \dots, y_t)$) g new feature vectors presenting the set of new training samples ($Y^{new} = (y^{new}_1, \dots, y^{new}_g)$) by means of interpolation techniques. In fact, three interpolation methods have been used: linear interpolation, cubic spline interpolation and Lagrange interpolation.

Algorithm 1: Oversampling

READ Y^{train}

FOR each row of the matrix Y^{train} i (For $i=1$ to dim)
 Present each value of the row i by a point.
 Compute the interpolation function.
 Generate new samples abscissas.
 Compute new training samples according to the evaluation of the interpolation function f in new abscissas.
 Save new values in Y^{new} .

ENDFOR

PRINT Y^{new}

Figure 1 shows the flowchart of the oversampling.

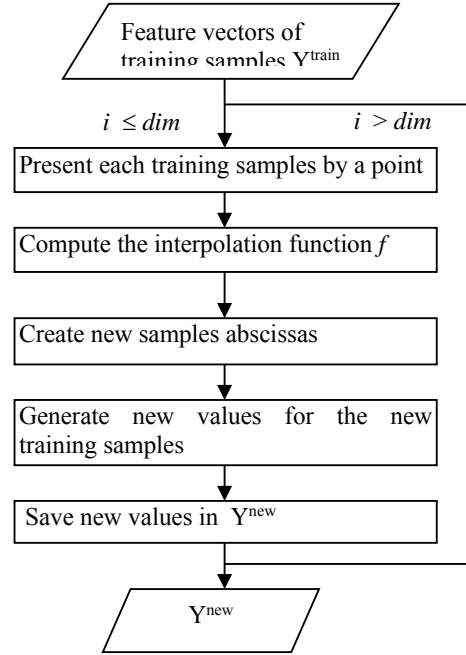


Figure 1: Flowchart of oversampling

3.3. Classification via SVM with multi-feature kernels

SVMs have been widely adopted in the classification of hyperspectral images due to their high performance registered on the process of data with high dimensionality. SVM [24] is a kernel based classifier consisting in projecting data in a higher dimension space by means of non-linear mapping function Φ and aiming at finding the optimal separator hyperplan by margin maximization. SVM has been proposed first for binary classification, after it has been introduced to solve multi-class classification.

In order to improve the classification performance achieved by using the spectral information alone, various spectral-spatial classification approaches incorporating the spatial information in addition to the spectral information have been proposed in the literature. In particular, the uses of SVM with kernels that combining different type of kernels like composite kernels [8] and multi-feature kernels [14] has shown high performance in term of accuracy.

In this paper, each pixel must be characterized by two spectral vectors x^{PCA} and x^{ICA} resulted respectively from the application of PCA et ICA and tree spatial vectors $x^{neighborhood}$, $x^{Texture}$ and x^{EMAP} computed respectively after the implementation of the mean of neighborhood pixels, textural features and EMAP. For that, we implemented tree different multi-feature kernels which combining these different spectral and spatial attributes:

- Kernel 1 (Equation (6)):

$$K^{PCA+ICA+Neigh+Text+EMAP}(x_i, x_j) = K_{PCA}(x_i^{PCA}, x_j^{PCA}) + K_{ICA}(x_i^{ICA}, x_j^{ICA}) + K_{Neigh}(x_i^{Neigh}, x_j^{Neigh}) + K_{Text}(x_i^{Text}, x_j^{Text}) + K_{EMAP}(x_i^{EMAP}, x_j^{EMAP}) \quad (6)$$



- Kernel 2 (Equation (7)):

$$\mu K^{PCA+ICA+Neigh+Text+EMAP}(x_i, x_j) = \mu \times [K_{PCA}(x_i^{PCA}, x_j^{PCA}) + K_{ICA}(x_i^{ICA}, x_j^{ICA})] + (1 - \mu) \times [K_{Neigh}(x_i^{Neigh}, x_j^{Neigh}) + K_{Text}(x_i^{Text}, x_j^{Text}) + K_{EMAP}(x_i^{EMAP}, x_j^{EMAP})] \quad (7)$$

with $0 < \mu < 1$.

- Kernel 3 (Equation (8)):

$$\alpha K^{PCA+ICA+Neigh+Text+EMAP}(x_i, x_j) = \alpha_1 \times K_{PCA}(x_i^{PCA}, x_j^{PCA}) + \alpha_2 \times K_{ICA}(x_i^{ICA}, x_j^{ICA}) + \alpha_3 \times K_{Neigh}(x_i^{Neigh}, x_j^{Neigh}) + \alpha_4 \times K_{Text}(x_i^{Text}, x_j^{Text}) + \alpha_5 \times K_{EMAP}(x_i^{EMAP}, x_j^{EMAP}) \quad (8)$$

$$\text{where } \sum_{i=1}^5 \alpha_i = 1.$$

To summarize the description of our proposed classification method, Algorithm 2 provides a pseudocode for our newly developed spectral spatial classification algorithm based on a SVM classifier with multi-feature kernels and oversampling.

Algorithm 2: SVM_oversampling

```

READ  $Y = (y_1, \dots, y_n)$  // Pixels of the hyperspectral image.
READ  $T$  // Set of training samples.
// Spectral characterization
 $Y^{PCA} = PCA(Y)$  // Compute the PCA of each pixels.
 $T^{PCA} = [T_1^{PCA}, \dots, T_c^{PCA}]$  // compute PCA of labeled pixels.
 $Y^{ICA} = ICA(Y)$  // Compute the ICA of each pixels.
 $T^{ICA} = [T_1^{ICA}, \dots, T_c^{ICA}]$  // compute ICA of learning pixels.
// Spatial characterization
 $Y^{Neigh} = Neigh(Y)$  // Calculate for each pixel the average of neighborhood pixels.
 $T^{Neigh} = [T_1^{Neigh}, \dots, T_c^{Neigh}]$  // Average of neighborhood pixels of training samples.
 $Y^{EMAP} = EMAP(Y)$  // Compute the EMAP of each pixels.
 $T^{EMAP} = [T_1^{EMAP}, \dots, T_c^{EMAP}]$ :
 $Y^{Text} = Text(Y)$  // Compute the textural features the of each pixels.
 $T^{Text} = [T_1^{Text}, \dots, T_c^{Text}]$  //

FOR each class  $i$ 
     $Y_{i\text{ new}}^{PCA} = \text{oversampling}(T_i^{PCA})$ 
     $Y_{i\text{ new}}^{ICA} = \text{oversampling}(T_i^{ICA})$ 
     $Y_{i\text{ new}}^{Neigh} = \text{oversampling}(T_i^{Neigh})$ 
     $Y_{i\text{ new}}^{EMAP} = \text{oversampling}(T_i^{EMAP})$ 
     $Y_{i\text{ new}}^{Text} = \text{oversampling}(T_i^{Text})$ 
// Spectral and spatial features of training samples after oversampling.
    
```

$$T_i^{PCA} = [T_i^{PCA}, Y_{i\text{ new}}^{PCA}]$$

$$T_i^{ICA} = [T_i^{ICA}, Y_{i\text{ new}}^{ICA}]$$

$$T_i^{Neigh} = [T_i^{Neigh}, Y_{i\text{ new}}^{Neigh}]$$

$$T_i^{EMAP} = [T_i^{EMAP}, Y_{i\text{ new}}^{EMAP}]$$

$$T_i^{Text} = [T_i^{Text}, Y_{i\text{ new}}^{Text}]$$

// Features of training samples in all the classes.

$$T_{\text{new}}^{PCA} = [T^{PCA}, T_i^{PCA}]$$

$$T_{\text{new}}^{ICA} = [T^{ICA}, T_i^{ICA}]$$

$$T_{\text{new}}^{Neigh} = [T^{Neigh}, T_i^{Neigh}]$$

$$T_{\text{new}}^{EMAP} = [T^{EMAP}, T_i^{EMAP}]$$

$$T_{\text{new}}^{Text} = [T^{Text}, T_i^{Text}]$$

ENDFOR

$L = SVM_Classification(Y^{PCA}, Y^{ICA}, Y^{Neigh}, Y^{EMAP}, Y^{Text}, T_{\text{new}}^{PCA}, T_{\text{new}}^{ICA}, T_{\text{new}}^{Neigh}, T_{\text{new}}^{EMAP}, T_{\text{new}}^{Text})$ // SVM classification with multi-feature kernels.

PRINT L // Labels of each pixel.

Figure 2 illustrate the flowchart of algorithm 2. The architecture of the proposed approach is illustrated in figure 3.

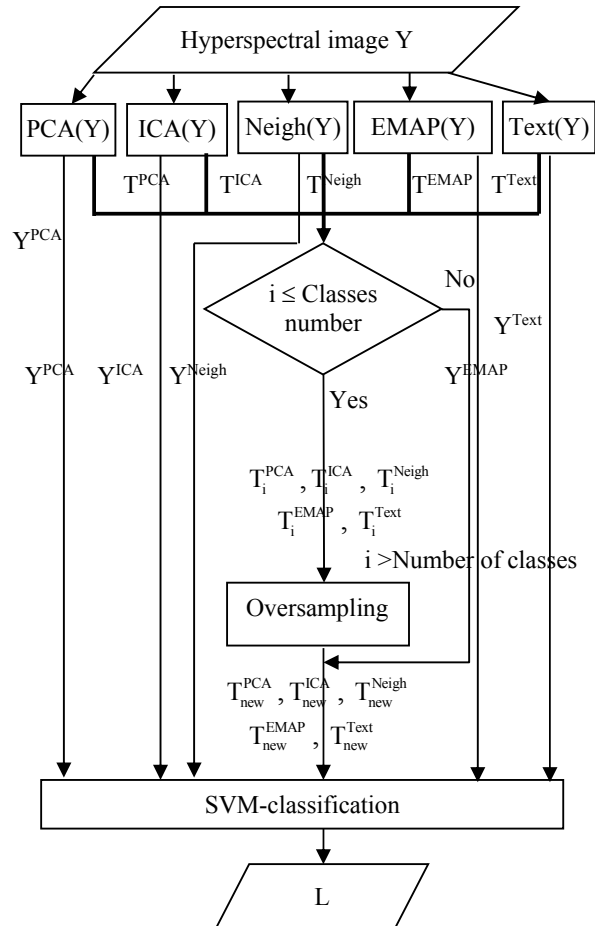


Figure 2: The flowchart of algorithm 2.



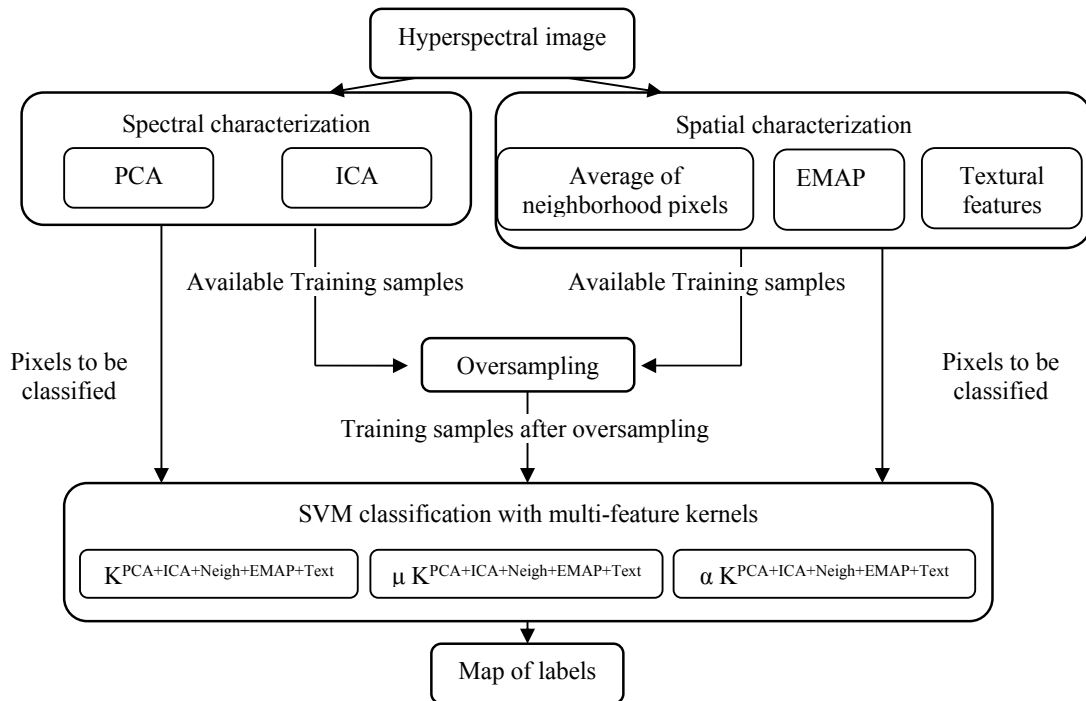


Figure 3: Architecture of the proposed approach.

3. Experimental results

To evaluate the performance of the proposed approach, we classified the widely used hyperspectral image "Indian Pines". It contains 145×145 pixels and 200 spectral bands. The ground-truth data contains 16 classes and a total of 10366 labeled pixels. The classification of this image is a challenging task refer to the significant presence of classes with similar spectral signatures and also because of the unbalanced number of available labeled pixels per class.

In all these experiments, we will use the classification accuracy (OA) and kappa coefficient (Kappa) as a references to evaluate the performance of the proposed classification approach.

For SVM classification, we implemented the most used multi-class classification strategy "one against all" and we used RBF and polynomial kernels for the spectral and spatial features, respectively, to construct multi-feature kernels. The training sets are randomly selected from the available labeled samples and that the remaining samples are used for validation. We optimized the SVM parameters using tenfold cross-validation.

After the spectral and the spatial characterization, each pixel has been presented by five vectors:

- \mathbf{x}^{PCA} is a spectral vectors that contains the first five principals components.
- \mathbf{x}^{ICA} is a spectral vector containing the six independents components.
- $\mathbf{x}^{\text{Neigh}}$ is a spatial vector that contains the average of neighborhood pixels in a window of size 3×3 .
- \mathbf{x}^{EMAP} a spatial vector that contains the EMAP of each pixel. EMAP were built according to the used attributes and thresholds presented in [25]: threshold values in the range of 2,5% - 10% with a step of 2,5% for the standard

deviation attribute and thresholds of 200, 500 and 1000 for the area attribute.

- \mathbf{x}^{Text} is a spatial vector that contains the textural features computed from the first three principals components. Note that we applied tree sliding windows: 3×3, 9×9 and 15×15 and we used four directions to calculate these features (LM, VAR, ASM and ENT).

Must indicate that the number of the used principals components in x^{PCA} and the number of the adopted independents components for x^{ICA} have been experimentally fixed according to the spectral classification of the image when using 10 labeled samples in each class (Figure 4).

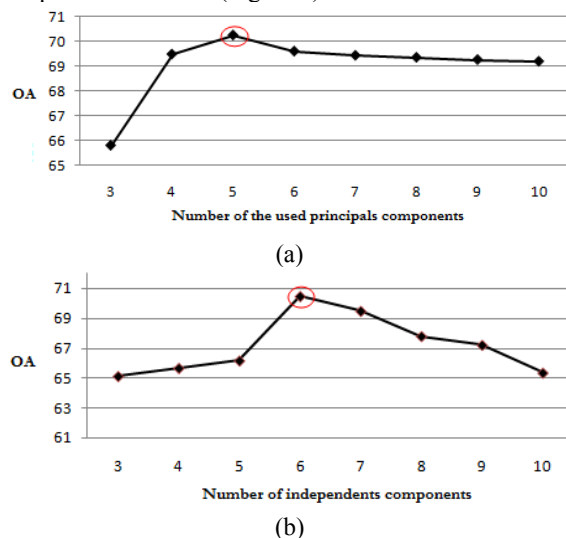


Figure 4. OA variation according to the variation of the number of principal components (a) and the number of independent components (b).



In order to analyze the impact of the multi-feature kernel and to select the most suitable for the classification of the "Indian Pines" data set, we analyze the performance of the proposed method for the tree kernels: $K^{PCA+ICA+Neigh+Text+EMAP}$, $\mu K^{PCA+ICA+Neigh+Text+EMAP}$ and $\alpha K^{PCA+ICA+Neigh+Text+EMAP}$ in a classification with generating in each class 10 samples about 10 available training samples. Figure 5 shows the OAs and kappa obtained by the proposed classification algorithm according to the applied kernels. Note that we used $\mu=0.25$ for $\mu K^{PCA+ICA+Neigh+Text+EMAP}$ and $(0.1,0.1,0.2,0.2,0.4)$ for $\alpha K^{PCA+ICA+Neigh+Text+EMAP}$. This chose has been fixed experimentally (Figure 6). As shown in Figure 3, the performance of the proposed classification algorithm increases when using $\alpha K^{PCA+ICA+Neigh+Text+EMAP}$ which valorize the spatial features extracted by EMAP ($\alpha_5=0.4 > \alpha_3=\alpha_4=0.2 > \alpha_1=\alpha_2=0.1$), it yielded much better OA and kappa results (OA= 82% and kappa=81,73%). Furthermore, we can note that the weighted summation kernel introducing a trade-off (μ) between spectral and spatial kernels with $\mu=0.25$ performs more accurately than the direct summation kernel.

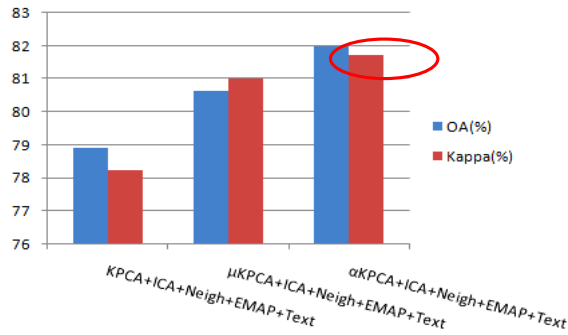


Figure 5: Resulted OA and Kappa coefficient according to the adopted multi-feature kernel

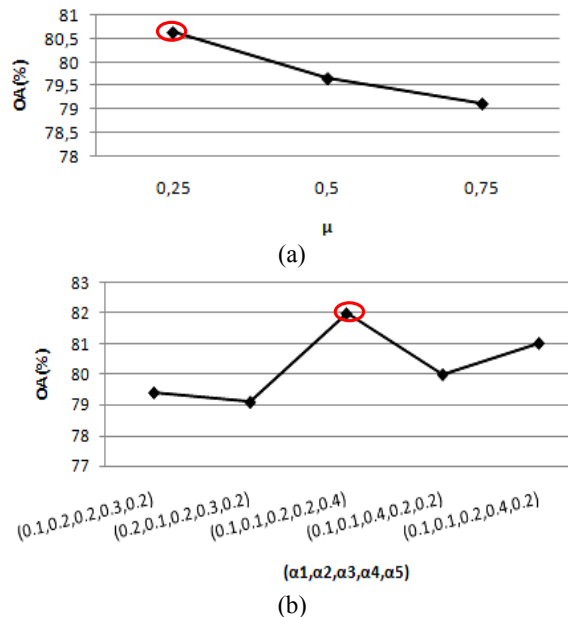


Figure 6: Variation of OA according to the variation of μ for the kernel $\mu K^{PCA+ICA+Neigh+Text+EMAP}$ (a) and $(\alpha_1, \alpha_2, \alpha_3, \alpha_4, \alpha_5)$ for the kernel $\alpha K^{PCA+ICA+Neigh+Text+EMAP}$ (b).

To show the advantage of the oversampling, we note in Table I the classification results obtained for different number of training samples after oversampling and without oversampling. In this experiment, we used cubic spline interpolation for the spectral and the spatial features to create new labeled samples and we adopted $\alpha K^{PCA+ICA+Neigh+EMAP+Text}$ as a multi-feature kernel.

Table I illustrate the average of the OA followed by the standard deviation (\pm) and the kappa coefficient obtained after ten Monte Carlo runs. By adopting oversampling, the proposed method significantly improved the classification results obtained by the considered classification without oversampling for all the adopted size of training set (10, 20 and 30). For instance, the generation of 40 samples about 10 labeled examples obtained an OA of 85.09%, 6.09% larger than that obtained by SVM without oversampling. As a result, the obtained samples after oversampling improves the accuracy of the supervised classifier (SVMs with multi-feature kernel). Notice also that the increase in the number of generated data improves significantly the performance of the classification (Figure 7) which indicates the advantage these samples that increase the ability of SVM to find the optimal separator hyperplan.

Table 1: OA and kappa coefficient (in parenthesis) obtained for the Indian Pines data set

Labeled samples	Number of generated samples				
	0	10	20	30	40
10	79% ± 1.3 (0.789)	81.32% ± 1.25 (0.81)	82.5% ± 1.4 (0.821)	84.04% ± 0.54 (0.83)	85.09% ± 0.64 (0.849)
20	85.56 ± 1.2 (0.86)	87.86 ± 1.11 (0.878)	88.39% ± 0.66 (0.89)	89.54% ± 0.67 (0.9)	90.34% ± 1.1 (0.91)
30	87.68 ± 0.92 (0.85)	89.34% ± 1.07 (0.896)	90.19% ± 1.15 (0.907)	91.3% ± 1.1 (0.92)	92.11% ± 0.56 (0.93)

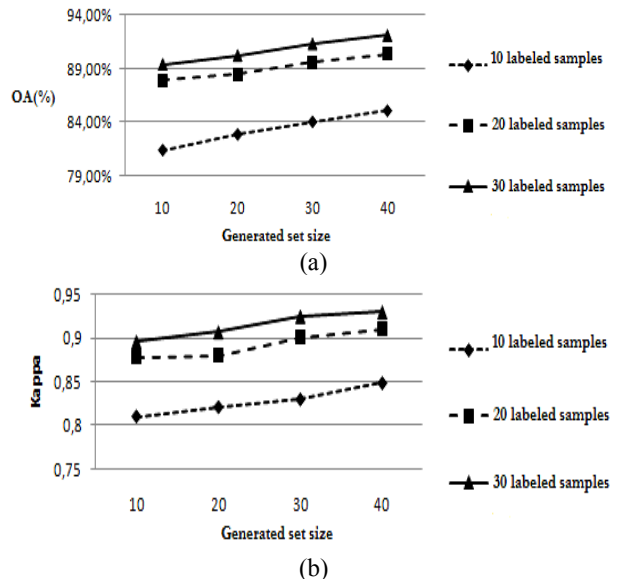


Figure 7: Variation of OA (a) and kappa coefficient (b) according to the increase in generated set size.



Focusing on the oversampling step, we have indicated in the description of the proposed classification method that we have implemented tree interpolation techniques to generate new training data: linear interpolation, cubic spline interpolation and Lagrange interpolation. Then to analyze the impact of these techniques and to select the most adequate for each feature, we note in table 2 the spectral, the spatial and the spectral-spatial classification results obtained after the generation of 20 data from 10 labeled samples by applying different interpolation methods. Table 2, illustrates for each interpolation method the OA, AA, kappa statistic coefficient (k), and individual class accuracy (in percent) results achieved by the spectral classification (two spectral classifications: using characteristics extracted by PCA and characteristics extracted by ICA), the spatial classification (tree spatial classifications: using characteristics extracted by the average of neighborhood pixels, textural features and characteristics extracted by EMAP) and the spectral-spatial classification assured by the proposed method. It is remarkable that the uses of Lagrange interpolation to create new spectral features (PCA, ICA) and spatial

features extracted by EMAP and the average of neighborhood pixels leads to have more accurate spectral and spatial classifications than that resulted after the application of the other methods: cubic spline and linear interpolation. For textural features, it's clear that the linear interpolation provided the highest accuracy. Then, for the spectral-spatial classification we applied the Lagrange interpolation for feature extracted by PCA, ICA, Neigh, and EMAP and the linear interpolation for the textural features. This combination provided high performance, it obtained an OA of 83.87% and kappa coefficient of 0,8385, 1.37% and 0.017 larger than these obtained when we used cubic spline interpolation for all features (indicated in table 1). This indicate that the samples generated by this combination are properly created refer to their similarity to the oversampled data in each class.

Figure 8 shows the ground truth and the classification result obtained without-oversampling and by the proposed method for the AVIRIS Indian Pines scene. The advantage of the proposed classification approach is clearly appreciable in this figure.

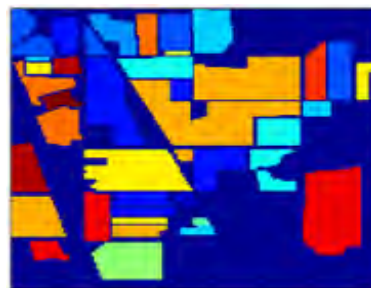
Table 2: Table 2: OA, AA an kappa coefficient obtained for the AVIRIS Indian Pines data set

Class	Test samples	Classification with oversampling								
		Spectral classification						Spatial classification		
		ACP			ACI			EMAP		
		Lin	Spl	Lag	Lin	Spl	Lag	Lin	Spl	Lag
Alfalfa	44	77,27	79,55	79,55	86,36	86,36	79,55	86,36	86,36	86,36
Corn-notill	1424	22,33	8,64	15,45	27,46	21,35	23,88	30,34	30,34	30,68
Corn-mintill	824	22,21	21	38,47	34,10	28,40	43,45	34,10	27,55	27,55
Corn	224	72,32	70,54	82,59	68,30	65,18	73,21	41,07	49,55	49,55
Grass/pasture	487	68,38	65,50	58,11	84,80	82,75	75,15	82,75	82,75	82,75
Grass/trees	737	81,68	84,12	86,43	83,18	88,60	87,38	87,89	87,89	85,89
Grass/pasture-mowed	16	81,25	87,50	87,50	68,75	87,50	87,50	93,75	93,75	93,75
Hay-windrowed	479	88,10	89,14	81	66,39	68,89	89,77	91,65	91,65	91,65
Oats	10	90	90	100	80	90	100	100	90	100
Soybean-no till	958	43,63	46,56	34,76	15,76	48,33	13,47	48,15	48,15	55,5
Soybean-min till	2458	51,51	31,08	44,26	48,41	8,01	57,28	48,70	48,70	48,70
Soybean-clean till	604	43,21	36,26	44,87	45,20	26,16	64,57	66,23	66,23	66,23
Wheat	202	63,37	74,75	79,70	52,97	56,93	68,81	95,05	95,05	95,05
Woods	1284	28,27	47,51	47,90	47,66	52,65	58,18	75,86	75,86	75,86
Bldg-Grass-Trees-Drives	370	40	62,16	50,81	18,92	26,22	20,54	62,16	71,35	71,35
Stone-Steel-Towers	85	91,76	91,76	97,65	90,59	91,76	91,76	91,76	97,65	97,65
OA (%)		69,59	68,84	70,59	68,43	66,61	71,44	72,11	72,98	74,02
AA (%)		61,63	61,63	64,32	57,43	58,07	64,66	69,82	70,67	71,15
kappa		0,6026	0,5872	0,6089	0,6152	0,6181	0,67	0,721	0,721	0,721

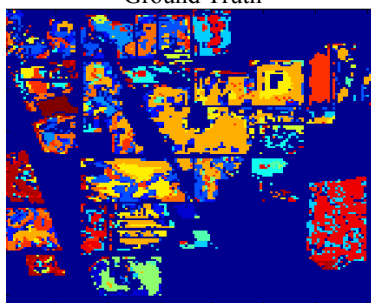
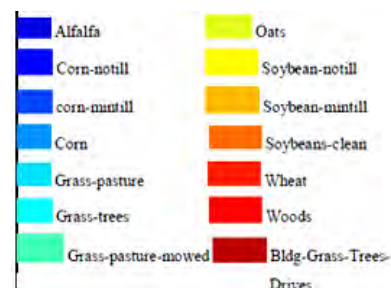


Table 2 (suite)

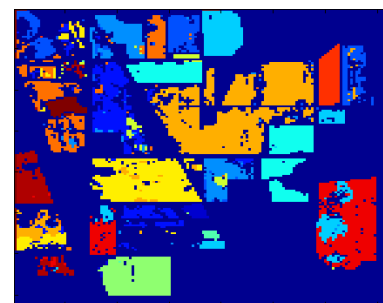
Class	Test sam ples	Classification with oversampling							
		Spatial classification						Multi-feature classification	
		Neighborhood			Textural features				
		Lin	Spl	Lag	Lin	Spl	Lag	Without oversampling	Lag_Lag_Lag_ Lag_Lin
Alfalfa	44	88,64	86,36	86,36	84,09	88,64	84,09	90,91	93,18
Corn-notill	1424	19,87	21,14	22,68	9,27	13,41	10,60	30,34	38,97
Corn-mintill	824	28,28	31,92	27,55	16,38	17,23	24,51	34,59	57,28
Corn	224	45,54	41,52	49,55	41,07	41,07	37,05	82,59	87,05
Grass/pasture	487	47,23	45,38	60,57	44,35	40,66	35,93	74,33	82,96
Grass/trees	737	82,77	81,82	85,89	31,34	31,48	27,68	89,69	93,49
Grass/pasture-mowed	16	93,75	93,75	93,75	81,25	87,50	87,50	87,50	87,50
Hay-windrowed	479	94,36	93,53	91,65	59,71	60,54	55,74	92,28	95,82
Oats	10	100	100	100	80	80	90	100	100
Soybean-no till	958	49,16	49,69	49,58	27,56	34,66	43,01	55,22	68,06
Soybean-min till	2458	48,58	48,17	48,70	45,77	45,36	42,35	52,73	59,72
Soybean-clean till	604	70,03	69,04	66,23	40,89	30,79	39,57	50,83	62,42
Wheat	202	95,05	95,54	95,05	85,15	90,10	86,63	98,51	99,01
Woods	1284	63,16	72,98	75,86	69,55	63,24	64,49	62,31	62,69
Bldg-Grass-Trees-Drives	370	70,27	71,62	71,35	73,78	63,24	54,59	45,68	65,95
Stone-Steel-Towers	85	100	100	97,65	98,82	98,82	100	98,82	98,82
OA (%)		70,83	71,5	73,12	69,02	65,16	67,62	78,79	83,87
AA (%)		68,54	68,91	70,15	55,56	55,42	55,23	71,64	78,31
kappa		0,574	0,5944	0,6187	0,475	0,4657	0,4662	0,78	0,8385



Ground Truth



Without oversampling 78,79%



With oversampling 82,87%

Figure 8: Classification maps obtained for the AVIRIS Indian Pines scene



4. Conclusion

In this paper, we have presented a new spectral-spatial classification approach which combines various spectral and spatial features via multi-feature kernels and generate new training samples to solve two problems widely proposed in the classification of hyperspectral images which are the difficulty of the choice of the applied characterization methods and the availability of a limited number of labeled samples. It investigates the oversampling based on interpolation techniques to increase the size of training set. By using the kernel $\alpha K^{PCA+ICA+Neigh+Text+EMAP}$ which valorize the spatial features computed by EMAP and by adopting the Lagrange interpolation for features extracted by PCA, ICA, the average of neighborhood pixels and EMAP and the linear interpolation for textural features in the oversampling step, the proposed method provides good accuracies when compared with the spectral classification, the spatial classification and the classification without oversampling. Combining multi-feature kernels and oversampling provides competitive and encouraging results. Further work should be focused on the exploitation of active learning algorithms to improve the quality of the generated samples in the oversampling step.

5. References

- [1] F. M. Lacar, M. M. Lewis, and I. T. Grierson, "Use of hyperspectral imagery for mapping grape varieties in the Barossa Valley, South Australia," in *IEEE International Geoscience and Remote Sensing Symposium 2001 (IGARSS '01)*, vol. 6, pp. 2875–2877, 2001.
- [2] E. K. Hege et al. "Hyperspectral imaging for astronomy and space surveillance," in *Proc. SPIE 5159, Imaging Spectrometry IX*, 380, 2004.
- [3] P.W. Yuen and M. Richardson, "An introduction to hyperspectral imaging and its application for security, surveillance and target acquisition," *The Imaging Science Journal*, vol. 58, no. 5, pp. 241–253, 2010.
- [4] J. B. Dias et al., "Hyperspectral remote sensing data analysis and future challenges," *IEEE Geoscience and Remote Sensing Magazine*, vol. 1, no. 2, pp. 6–36, 2013.
- [5] H. Zhang, J. Li, Y. Huang, and L. Zhang, "A nonlocal weighted joint sparse representation classification method for hyperspectral imagery," *IEEE Journal of Selected Topics in Applied Earth Observations and Remote Sensing*, vol. 7, no. 6, pp. 2056–2065, Jun. 2014.
- [6] H. Yuan, Y. Yan Tang, Y. Lu, L. Yang, and H. Luo, "Hyperspectral image classification based on regularized sparse representation," *IEEE Journal of Selected Topics in Applied Earth Observations and Remote Sensing*, vol. 7, no. 6, pp. 2174–2182, Jun. 2014.
- [7] G. Camps-Valls, L. Bruzzone, "kernel methods for remote Sensing data analyzes", *J.wiley and Sons*, NJ, USA, 2009.
- [8] G. Camps-Valls, L. Gomez-Chova, J. Munoz-Mari, J. Vila-Frances, and J. Calpe-Maravilla "Composite Kernels for Hyperspectral Image Classification", *IEEE geoscience and remote sensing letters*, vol.3, no.1, pp. 93 - 97, Jan. 2006.
- [9] M. Fauvel, J. A. Benediktsson, J. Chanussot and J.R. Sveinsson " Spectral and Spatial Classification of Hyperspectral Data Using SVMs and Morphological Profiles", *IEEE transaction on geoscience and remote sensing*, vol.46, no.11, pp. 3804 - 3814, Nov. 2008.
- [10] X. Kang, S. Li and J. A. Benediktsson "Spectral-spatial Hyperspectral Image Classification with Edge-preserving Filtering", *IEEE transactions on geoscience and remote sensing*, vol. 52 , no. 5, pp. 2666 - 2677, May 2014.
- [11] X. Huang and L. Zhang "An SVM Ensemble Approach Combining Spectral, Structural, and Semantic Features for the Classification of High-Resolution Remotely Sensed Imagery", *IEEE transactions on geoscience and remote sensing*, vol. 51, no. 1, pp. 257 - 272, Jan. 2013.
- [12] J. Li, P. R. Marpu, A. Plaza, J. M. Bioucas-Dias and J. A. Benediktsson " Generalized Composite Kernel Framework for Hyperspectral Image Classification", *IEEE transactions on geoscience and remote sensing*, vol. 51, no. 9, pp. 4816 - 4829, Sep. 2013.
- [13] P. Ghamisi, M. S. Couceiro, M. Fauvel and J. A. Benediktsson "Integration of Segmentation Techniques for Classification of Hyperspectral Images", *IEEE on geoscience and remote sensing letters*, vol. 11, no. 1, pp. 342-346, JANUARY 2014.
- [14] R. Ben Salem, K. S. Ettabaa and M. A. Hamdi " Spectral-spatial classification of hyperspectral images using different spatial features and composite kernels", in *IEEE International Image Processing, Applications and Systems Conference 2014 (IPAS'14)*, pp. 1- 7, Nov.2014.
- [15] Rodarmel and J. Shan " Principal Component Analysis for Hyperspectral Image Classification", *Surveying and Land Information Systems*, vol. 62, no. 2, pp.115-123 , 2002.
- [16] Q. Du "Independent component analysis to hyperspectral image classification", *Proc. SPIE 5546, Imaging Spectrometry X*, 366, Oct.2004.
- [17] M.D. Mura, J.A.Benediktsson, B; Waske, L. Bruzzone, "Extended profiles with morphological attribute filters for the analyses of hyperspectral data," *Int. J. Remote sens.*, vol. 31, no. 22, pp.5975-5991, Jul. 2010
- [18] X. Huang, L. Zhangaand P. Lia " A multiscale feature fusion approach for classification of very high resolution satellite imagery based on wavelet transform", *International Journal of Remote Sensing*, vol. 29, no. 20, pp. 5923-5941, Oct. 2008.
- [19] X. Huang, L. Zhang and P. Li" An Adaptive Multiscale Information Fusion Approach for Feature Extraction and Classification of IKONOS Multispectral Imagery Over Urban Areas", *IEEE on geoscience and remote sensing letters*, vol. 4, no. 4, pp. 654 - 658, Oct. 2007.
- [20] S. Serpico and G. Moser, "Extraction of spectral channels from hyperspectral images for



- classification purposes," IEEE Trans. Geosci. Remote Sens., vol. 45, no. 2, pp. 484-495, Feb. 2007.
- [21] R. Ben Salem, K. Saheb Ettabaa and M. A. Hamdi" Supervised spectral-spatial hyperspectral image classification based on oversampling and composite kernels", ICGST-GVIP, vol.15, no.2, pp.27-39, Dec. 2015.
- [22] M. Volpi, D. Tuia, F. Bovolo, M. Kanevski, L. Bruzzone " Supervised change detection in VHR images using contextual information and support vector machines", International Journal of Applied Earth Observation and Geoinformation, vol. 20, pp. 77-85, 2013.
- [23] M.D. Mura, J.A.Benediktsson, B. Waske, L. Bruzzone, "Extended profiles with morphological attribute filters for the analyses of hyperspectral data," Int. J. Remote sens., vol. 31, N. 22, pp.5975-5991, Jul. 2010.
- [24] G. Mercier, M. Lennon, " Support vector machines for hyperspectral image classification with spectral based kernels," International symposium on geoscience and remote sensing (IGARSS 2003), vol.1, pp. 288 - 290 , July 2003.
- [25] J.A. Benediktsson, J.A. Palmason et J.R. Sveinsson "Classification of hyperspectral data from urban areas based on extended morphological profiles", IEEE Transactions on Geoscience and Remote Sensing, vol. 43, no. 3, pp. 480-491, Mar. 2005.

Biographies



Rafika Ben Salem received the Eng. and M. degrees from National school of engineering, Sousse at 2009 and 2011. Currently she is a PhD student at National institute of applied sciences and technology, Tunis in the MMA Laboratory. Her research interests include remote sensing image interpretation and classification.



Karim Saheb Ettabaa received the M.E. and Dr. Eng. degrees from ENSI, Manouba, Tunisia, in 2004 and 2007, respectively. He is a Permanent Researcher at laboratory RIADI, National School of Computer Sciences Engineering and ITI, Telecom Bretagne, Brest Iroise Technopole CS 81828. His research interest includes image processing, data mining, artificial intelligence, pattern recognition, and their application to remote sensing



Mohamed Ali HAMDI received the Ph.D. degree in image processing, from the National University of engineering of TUNIS, He is Assistant Professor of Applied and Computational Mathematics and electronic, National institute of applied sciences and technology. His research interests are in the areas of digital signal processing (DSP), statistical estimation and their applications to signal and image processing and scientific computing.

